

COLORS AND SPECTRA OF KUIPER BELT OBJECTS ¹

David C. Jewitt²

Institute for Astronomy

2680 Woodlawn Drive, Honolulu, HI 96822

and

Jane X. Luu

Sterrewacht Leiden

Postbus 9513, 2300RA Leiden, The Netherlands

Received _____; accepted _____

Submitted to *Astronomical Journal*, May 2001

¹Based [in part] on data collected at Subaru Telescope, which is operated by the National Astronomical Observatory of Japan.

²Visiting Astronomer, W. M. Keck Observatory, jointly operated by California Institute of Technology and the University of California.

ABSTRACT

We present new measurements of the optical colors of Kuiper Belt Objects, principally from the Keck 10-m telescope. The measurements confirm the existence of a wide spread in the B-V, V-R and R-I color indices (Luu and Jewitt 1996). Relative to the sun, the Kuiper Belt Objects exhibit reflected colors from nearly neutral to very red. The optical and optical-infrared (V-J) color indices are mutually correlated, showing the presence of a single reddening agent from $0.45\mu m$ to $1.2\mu m$. On the other hand, we find no evidence for linear correlations between the color and absolute magnitude (a proxy for size), instantaneous heliocentric distance, semi-major axis, or with any other orbital property. In this regard, the Kuiper Belt Objects differ from the main-belt asteroids in which strong radial color gradients exist. We find no statistically significant evidence for bimodal or other non-uniform color distributions, either in our data, or in data previously reported to show such evidence. The impact resurfacing hypothesis is re-examined in the light of the new color data and is rejected as the primary cause of the observed color dispersion. We also present new near-infrared reflection spectra of 1993 SC, 1996 TS₆₆, 1999 DE₉ and 2000 EB₁₇₃, taken at the Keck and Subaru telescopes. These spectra, combined with others from the published literature, provide independent evidence for compositional diversity in the Kuiper Belt. Objects 2000 EB₁₇₃, 1993 SC, and 1996 TS₆₆ are spectrally bland while 1999 DE₉ shows solid-state absorption bands.

Subject headings: comets – Kuiper Belt – solar system: formation

1. Introduction

Ground-based surveys have revealed (as of July 2001) more than 400 Kuiper Belt Objects (KBOs). These bodies have orbital semi-major axes $a > 30$ AU and a wide range of orbital properties showing clear evidence for dynamical sub-structuring (Jewitt, Luu and Chen 1996; Luu et al. 1997; Jewitt, Luu and Trujillo 1998; Trujillo, Jewitt and Luu 2000). The inferred population of objects with diameters ≥ 100 km is of order 4×10^4 (in the classical belt; Trujillo, Jewitt and Luu 2001) while the inferred number of (mostly unseen) bodies larger than 1 km in diameter numbers many billions.

The Kuiper Belt is thought to be a relic from the earliest phases of the solar system. The low radiation equilibrium temperatures of KBOs ($T \approx 40 - 50$ K) allow the possibility that many common ices could be retained over the age of the solar system. Indeed, it is widely thought that the volatile-rich nuclei of most short-period (specifically, Jupiter-family) comets are escaped members of the Kuiper Belt while the Centaurs (bodies with perihelia and semi-major axes between the orbits of Jupiter and Neptune) represent an intermediate dynamical stage. There is strong interest in understanding the physical properties and compositional natures of the KBOs both as clues to the early solar system and as samples of cometary material relatively unchanged by heating by the sun. Unfortunately, most known KBOs are faint (apparent red magnitude $m_R \geq 22$) and their properties difficult to measure with accuracy. The most secure and, so far, uncontested observational result is that the KBOs exhibit diverse optical colors ranging from nearly neutral ($V-R \approx 0.3$) to very red ($V-R \approx 0.7 - 0.8$) (Luu and Jewitt 1996; Green *et al.* 1997; Tegler and Romanishin 1998; Barucci *et al.* 2000). A wide range in the V-J color index also appears well established (Jewitt and Luu 1998; Davies *et al.* 2000; Noll, Luu and Gilmore 2000).

Two qualitative explanations for the color diversity of KBOs have been proposed (Luu and Jewitt 1996). First, color differences might result from the competition between cosmic

ray bombardment (which may tend to produce a low albedo, reddish reflectivity) and occasional impact excavation of sub-surface volatiles. The resurfacing hypothesis makes specific predictions about the color distribution of the KBOs and is therefore testable. Resurfacing is only effective as a cause of spectral diversity when the timescales for irradiation darkening and impact resurfacing are comparable. The resulting surfaces of the KBOs should occupy a continuum of states from fully mantled, low albedo and reddish at one end to fully resurfaced, ice covered and neutral at the other. Furthermore, since not all resurfacing events would globally coat KBOs with excavated material, a second prediction is that the colors (and spectra) of KBOs should be azimuthally variable. A third prediction is that the rotationally averaged colors of the KBOs should systematically vary with the object size, since small bodies have shorter resurfacing times than larger ones while the cosmic ray reddening timescale is independent of size (c.f. Figure 4 of Luu and Jewitt 1996).

Alternatively, color diversity could simply indicate intrinsically different compositions among the KBOs. This second hypothesis is difficult to reconcile with the relatively small temperature gradients expected across the trans-Neptunian solar system. In radiative equilibrium with the sun, the local blackbody temperature varies as $T(R) \approx 278R^{-1/2}$, where R [AU] is the heliocentric distance. The temperature difference from 30 AU to 50 AU is a paltry 11 K, scarcely enough to affect the chemical composition of the KBOs. Slightly larger temperature gradients might be expected if the KBOs have been swept outward from their formation locations by the radial migration of Neptune, but still it is difficult to see how the bulk composition could be substantially affected. Nevertheless, in view of the uncertainties in the modes of formation and dynamical histories of the KBOs, the second hypothesis cannot yet be ruled out as a viable explanation of the color distributions of the KBOs.

Tegler and Romanishin (1998 and 2000, hereafter TR98 and TR00) reported a bimodal

distribution of KBO colors. Independently, Barucci *et al.* (2001) refute this bimodality but report evidence for four distinct color groups within the KBO population. Bimodal and multi-modal distributions are interesting in the present context because they cannot be produced by stochastic resurfacing. The question of whether the KBO color distribution is unimodal or bimodal therefore confronts the resurfacing hypothesis. While a number of authors have published color measurements that specifically refute the bimodal distribution (Barucci *et al.* 2000, Davies *et al.* 2000), it is in fact difficult to imagine how such a distribution could be produced as an artifact. For example, low quality photometry having large uncertainties will tend to blur a bimodal distribution into a unimodal one, not the other way round. This raises the possibility that Tegler and Romanishin’s careful use of aperture correction techniques in photometry could be responsible for their detecting bimodality while others do not see it (Barucci *et al.* 2000 used aperture correction but their sample included only eight objects). We investigate this possibility in Section 2.

In this paper, we present new optical photometry of 26 KBOs and 2 Centaurs taken at the Keck and University of Hawaii telescopes. The new measurements constitute a single data set relatively free of systematic errors that might afflict conclusions drawn by comparing photometry from different sources. In addition, we present new reflection spectra of four KBOs in the near infrared ($1\mu\text{m} \leq \lambda \leq 2.4\mu\text{m}$) wavelength range. We ask the following questions:

1. Are the optical colors bimodally distributed?
2. Are the optical and optical-near-infrared colors correlated?
3. Are there correlations between surface color and physical or orbital properties of the KBOs?
4. Are the available data compatible with the resurfacing hypothesis?

5. What clues are provided by the spectral evidence?

2. Optical Observations

Optical observations were obtained under photometric conditions at the Keck II telescope using the LRIS imaging camera (Oke *et al.* 1995). This camera incorporates a Tektronix 2048 x 2048 pixel charge-coupled device (CCD) and gives an image scale of 0.215 arcsec per $24\mu\text{m}$ pixel. Facility broadband BVRI filters were used for all observations. Photometric calibration of the data was obtained through observations of standard stars on the Johnson-Kron-Cousins photometric system (Landolt 1992). The images were processed using flat fields calculated from the nightly medians of bias-subtracted data taken through each filter. The resulting images were found to be uniform in sensitivity across the width of the CCD to better than 1%, with the largest deviations occurring near the east and west edges of the field of view, in a region that was partially vignetted by the LRIS optics. All target objects and standard stars were placed within 300 pixels of the center of the field of view (FOV) and completely avoided the vignetting. The images were autoguided at sidereal rates. We used short integration times (from 200 sec to 500 sec) in order to minimise trailing of the KBOs relative to the stars. At opposition, the KBOs trail ~ 0.4 arcsec in 500 sec, which is small compared to the 0.7 - 1.0 arcsec Full Width at Half Maximum (FWHM) seeing in most of our data.

Additional optical observations of four bright KBOs were obtained at the University of Hawaii 2.2-meter telescope. We used a Tektronix 2048×2048 pixel CCD camera at the $f/10$ Cassegrain focus to obtain a 7.5×7.5 arcmin² FOV and a 0.219 arcsecond/pixel image scale. Flat fielding and photometric calibration were obtained as at the Keck telescope.

2.1. Profile Correction

There are several sources of uncertainty in the photometry and, in view of the importance of the errors, it seems worthwhile to discuss them here. The main problem is that, while large photometry apertures are needed to capture all the light in the point spread function (PSF), large apertures also capture a large (and noisy) signal from the background sky. Specifically, if the function $f(a)$ ($Wm^{-2}Hz^{-1}(arcsec)^{-2}$) represents the PSF, the total flux within the PSF measured out to radius a [arcsec] is simply

$$F(a) = \int_0^a 2\pi a f(a) da, \quad (1)$$

while the flux in the background measured out to the same radius is

$$F_b(a) = \int_0^a 2\pi a f_b da = \pi a^2 f_b, \quad (2)$$

where f_b ($Wm^{-2}Hz^{-1}(arcsec)^{-2}$) is the sky surface brightness. Ideally, we would like to measure $F(a \rightarrow \infty)$, to capture all of the light from the PSF but then background signal $F_b(a \rightarrow \infty) \rightarrow \infty$. For faint objects, the noise on the background sky completely dominates the photometric uncertainty. The tempting option is to use photometry from small apertures to reduce random errors caused by noise on the background signal. However, this introduces potentially devastating systematic errors due to the variable and unknown fraction of the total light captured within the small aperture.

We followed the example of TR98 and used photometry of field stars to empirically determine a profile correction, defined by

$$\Delta m_p = -2.5 \log \left[\frac{F(a_1)}{F(a_2)} \right]. \quad (3)$$

Here, a_1 and a_2 are the radii of the small and large photometry apertures used, respectively, to measure the KBOs and their reference field stars and the photometric standard stars. Essentially, Eq. (3) is a correction to be added to small-aperture measurements of KBO magnitudes to estimate the total flux density that would be obtained if low noise, large aperture measurements were possible. We experimented to determine optimal values of the aperture radii by trial and error, eventually selecting $a_1 = 1.00$ arcsec and $a_2 = 3.22$ arcsec for most measurements. The median sky signal was determined from a contiguous annulus 4 to 5 arcsec wide. Typically 5 - 10 field stars were identified in each image and used to determine Δm_p . In practice, we found two important limitations to this procedure. First, the PSF of the Keck data varies slightly with position on the CCD. We selected field stars near the target KBOs to reduce the effect of spatial variations. Second, in the fine seeing above Mauna Kea we could see that most of the field objects were marginally resolved galaxies and, in some fields, we had difficulty locating a suitable number of stars with which to determine Δm_p . With the above parameters, we found $\Delta m_p = 0.3$ to 0.5 mag, depending on the seeing. The uncertainty on Δm_p determined from the dispersion among measurements of different field stars was typically $\sigma_p = 0.01 - 0.03$ mag.

2.2. Noise Properties of the Data

We examined the effects of background fluctuations on the photometry by placing artificial KBOs on the CCD and measuring their magnitudes using procedures identical to those employed for real objects. The PSFs of the artificial KBOs were matched to the PSFs of the real data on an image-by-image basis, including allowance for non-zero ellipticity (e.g., caused by wind shake) where appropriate. Measurements of about 20 artificial objects were used to calculate the empirical standard deviation within each of several magnitude bins. A sample image is shown in Fig. 1, for the particular case of 1996

SZ4. In background-limited observations, the photometric uncertainty, σ_B , should vary with the magnitude of the source, m_R , as

$$\sigma_B = -2.5 \log [1 + \kappa 10^{0.4m_R}] \quad (4)$$

where κ is a constant that depends on the surface brightness of the night sky and the integration time. We find that Equation (4) provides an acceptable fit to the measurements in each filter (Fig. 2). The combined uncertainty is estimated from

$$\sigma = \sqrt{(\sigma_B^2 + \sigma_p^2)}. \quad (5)$$

The above error treatment accounts for contamination by background sources in a statistical sense. The photometry can potentially still suffer from contamination by rare, bright background sources that are not well sampled by the above procedure. Most such sources are distant galaxies, typically extended on scales comparable to the seeing. For example, a galaxy of red magnitude $m_R = 25$ constitutes a 2.5% (6.5%) error signal to a foreground KBO of magnitude $m_R = 21(22)$. We used the motion of KBOs between images to provide protection from such background objects. Photometry that was obviously compromised was rejected from the sample.

2.3. Photometric Results

The geometrical circumstances of the observations are summarised in Table 1. The optical photometry is listed in Table 2 while color-color plots are shown in Figures 3, 4 and 5. For reference, the corresponding colors of the Sun are approximately given by $B - V = 0.67$, $V - R = 0.36$, $R - I = 0.35$, $V - J = 1.08$ (Hartmann, Cruikshank and Degewij 1982, Hartmann *et al.* 1990). The solar colors are marked in Figures 3 - 5. We note immediately

from the Figures that the B-V, V-R and R-I color indices are redder than the Sun and are mutually correlated: objects that are red at B (4500Å wavelength) are also red at I (8500Å). Linear correlation coefficients are summarized in Table 3. In the Table, $P(r \geq r_{corr})$ denotes the probability that a correlation coefficient equal to or larger than the one measured could be produced by chance in random, uncorrelated data. $P(r \geq r_{corr}) = 0.003$ corresponds to the nominal 3σ criterion for a statistically significant correlation.

The color-color correlations are extended to longer wavelengths in Fig. 6, where we plot those objects observed in J band ($1.2\mu\text{m}$) from Jewitt and Luu (1998) and Davies *et al.* (2000). The B-I and V-J color indices are highly correlated (Table 3), suggesting that optical colors may be used as a proxy for the optical-near infrared V-J color. The correlations show that the reflectivities of the KBOs are consistent with a single reddening agent in the B ($0.45\mu\text{m}$) to J ($1.2\mu\text{m}$) regime. Spectra of many low albedo hydrocarbons show exactly this property (Cloutis *et al.* 1994). The reflectivity gradients at wavelengths greater than $1.2\mu\text{m}$ tend to be smaller, and are not well correlated with the optical gradients (Jewitt and Luu (1998), Davies *et al.* (2000)). A subset of the complex hydrocarbons also mimic this property, notably some coal tar extracts studied by Cloutis *et al.* (1994) and the Tholins (Cruikshank *et al.* 1998). The colors thus suggest, but do not uniquely diagnose, the presence of surface hydrocarbons.

The mean optical colors of the classical and resonant KBOs are indistinguishable (Table 4). The optical colors are correlated with neither the orbital nor physical properties of the KBOs (Table 3). If collisional effects are important, we might expect a correlation between KBO color and ΔV , the difference between the average velocity and the velocity of an uninclined, circular orbit of the same semi-major axis. We computed ΔV from the eccentricity and inclination of each of the observed KBOs, but find no statistically significant correlation with the $B - I$ color (Table 3). A V-J vs. semi-major axis correlation

was tentatively claimed by Weintraub *et al.* (1997) based on measurements of four Centaurs. In fact, this correlation is statistically insignificant ($P(N, r_{corr}) < 0.1$) and is unsupported by the new data (Table 3).

Some of the objects in our sample have been previously measured. We compare the new results with published data in Table 5. A graphical comparison of the measurements is shown in Figure 7. In general, the independent measurements agree within the combined uncertainties. For example, 5 of 19 objects (26%) have independently measured $V - R$ colors which are different by more than 1 combined standard deviation (1σ). This is consistent with a Gaussian error distribution, for which we expect about 32% of measurements to lie beyond 1σ . We summarise the data sets in Table 6. In terms of their extrema, means and dispersions, the color samples of TR98, TR00 and the present work are remarkably concordant (columns 3-5 in Table 6).

2.4. The Color Distribution

TR98 contend that the B-V and V-R colors are bimodally distributed. Their data, which include a mixture of Centaurs and KBOs, are plotted in Fig. 8. In a later work, Tegler and Romanishin 2000 reported observations of the B-V and V-R colors of 16 additional KBOs and 3 Centaurs (Fig. 9). They reported that the color distribution remained bimodal with the addition of the new data, although this is visually less obvious (compare Fig. 8 with Fig. 9). Tegler and Romanishin did not assess the statistical significance of the bimodality in either of their samples, and neither did they attempt to account for its physical origin. Clearly, a test of the significance of the reported bimodality is in order. We consider three such tests.

The Bin Test

Most of the dispersion among the colors in Figs. 8 and 9 occurs along a line of principal variation that is slightly inclined relative to the B-V axis. We use the position of each KBO measured along this line, defined by

$$C = [(B - V)^2 + (V - R)^2]^{1/2} \quad (6)$$

to test the null hypothesis that the colors are distributed randomly along the line. The probability that, in a sample of n measurements distributed randomly among k equal-sized bins, the central bin will hold m objects is given by

$$P(n, m) = \left[\frac{n!}{m!(n - m)!} \right] p^m (1 - p)^{n - m} \quad (7)$$

where $p = 1/k$. We present calculations for three bins ($k = 3$) with C in the range $0.65 \leq C \leq 1.55$. Table 6 lists the number of objects in the central bin, which has $0.95 \leq C \leq 1.25$, for each sample.

Evaluation of the probabilities using Eq. (7) shows that the TR98 sample has roughly a 3% likelihood of having been drawn by chance from a uniform distribution, corresponding to a result that is $\approx 2.2\sigma$ in statistical significance. Tegler and Romanishin’s larger second sample (TR2000) is even less significantly bimodal (with a 13% probability of having been derived from a uniform distribution), as is the sample from the present work (for which the probability is also about 13%: Table 6). In fact, the combined TR98 + TR00 data sets are comparable to the data set from the present work in terms of size, range, mean, standard deviation on the mean, and the lack of evidence for a bimodal distribution of colors (Table 6). In all, we find that the data present a remarkably coherent case for a distribution of colors that is devoid of evidence for bimodality.

The bin test has been recomputed for other values of C_{min} , C_{max} and k , but always with the results that a) the most significant (but still $< 3\sigma$) evidence for bimodality is in the TR98 data and b) the significance of bimodality decreases as the sample size increases. We conclude that the bin test provides no evidence that the $B - V$ or $V - R$ colors are distributed bimodally.

The Dip Test

As another test for bimodality, we make use of the dip statistic (Hartigan and Hartigan 1985), which is defined as the maximum difference between the (perhaps bimodal) data distribution and the unimodal distribution function that minimizes that maximum difference. In effect, the test tries to explain the data distribution with a best-fitting unimodal distribution, and the dip statistic is the residual from matching the two functions. The larger the dip the larger the mismatch. Hartigan and Hartigan’s test computes the dip statistic then evaluates its significance. The results upon performing the dip test on Tegler and Romanishin’s data and our own data (this work) are presented in Table 7. In agreement with visual impressions (Figure 8), the most nearly significant evidence for bimodality is in $V - R$ from TR98 but this is still $< 3\sigma$ and not supported by the TR00 or present $V - R$ measurements. The dip test, like the bin test, provides no evidence in support of bimodality.

The Interval Distribution Test

We lastly consider the distribution of intervals between KBO color measurements. In a truly bimodal distribution, there should be a large interval (between modes) followed by many smaller intervals (between the members of each mode). Conversely, in a continuous distribution, one expects all intervals to be roughly equal. To assess the likelihood that the

large interval observed in Tegler and Romanishin’s color distribution might arise by chance from random, uncorrelated data, we computed Monte Carlo models in which we randomly picked colors from a uniform distribution, then determined the largest interval, LI , between two consecutive colors. We repeated this experiment 10^5 times in order to determine the probability of obtaining a given LI by random chance, given n data points. We selected colors in the ranges $0.60 \leq B - V \leq 1.30$ and $0.35 \leq V - R \leq 0.80$, respectively. For illustration, we present the results of our experiments in Figs. 10 and 11, where we plot the LI cumulative probability distribution as a function of n for the $B - V$ and $V - R$ data sets.

The results of the interval distribution test are summarised in Table 8. There it can be seen that, at the canonical 3σ ($P = 0.3\%$) level of confidence, the measured values of LI are consistent with random sampling of a uniform color distribution. This is already qualitatively obvious in a comparison of Fig. 8 (TR98) with Fig. 9 (TR00). The gap in Fig. 9 is partially filled-in relative to the gap in Fig. 8, just as one expects from an enlarged data sample if the gap is merely a statistical fluctuation. A real gap in the color distribution would not shrink as the sample size increases.

We conclude that both our photometry and the photometry presented in two papers by Tegler and Romanishin are formally consistent with derivation from a uniform distribution of colors. Similarly, the distribution of optical-infrared ($V - J$) colors provides no hint of a bimodal distribution (Davies *et al.* 2000). These results are compatible with the original finding of Luu and Jewitt (1996) and with subsequent results presented by independent workers (Green *et al.* 1997, Barucci *et al.* 2000). Finding no significant evidence for bimodality, we next re-consider impact resurfacing as a possible cause of the observed unimodal color distribution.

3. Resurfacing Revisited

We have revisited the resurfacing mechanism taking into account improvements in the known parameters of the KBO size distribution that have accrued from our Mauna Kea surveys (Jewitt, Luu and Trujillo 1998, Trujillo, Jewitt and Luu 2001). The most important change that has occurred since Luu and Jewitt (1996) is the improved determination of the size distribution index. The Kuiper Belt Objects are distributed such that the number of objects with radii in the range a to $a + da$ is $n(a)da = \Gamma a^{-q}da$, with Γ and q constant. The best-fit index $q = 4.0_{-0.5}^{+0.6}$ (Trujillo, Jewitt and Luu 2001) is larger than the steepest models considered in Luu and Jewitt (1996). The total number of classical KBOs (CKBOs) larger than 100 km in diameter remains unchanged from our previous estimates, at $N_{CKBO} = 3.8_{-1.5}^{+2.0} \times 10^4$ (Trujillo, Jewitt and Luu 2001).

The collision rate onto a target KBO of radius a_T is

$$1/\tau \approx \int_{a_{min}}^{\infty} 4\pi(a_T + a)^2 \Delta V \psi n(a) da / W, \quad (8)$$

where ΔV is the velocity difference between the target and incoming projectiles, ψ is a dimensionless factor for gravitational focussing and W is the volume swept out by the orbits of the KBOs. Here, a_{min} is the radius of the smallest projectile. In practice, the integration extends to the largest KBO in the distribution (not to infinity!) but, given the steep size distribution, impacts by the largest objects are comparatively rare and the integration upper limit is not critical. We take $\Delta V = 1.3 \text{ km s}^{-1}$ (Trujillo, Jewitt and Luu 2001). The gravitational focussing is given by $\psi = 1 + (v_e/\Delta V)^2$, where v_e is the escape speed from the target object. For a spherical KBO of density $\rho [kg \text{ m}^{-3}]$, this may be expressed as

$$\psi = 1 + 8\pi G \rho a_T^2 / (3\Delta V^2) \quad (9)$$

Substituting $\Delta V = 1.3 \text{ km s}^{-1}$, $\rho = 10^3 \text{ kg m}^{-3}$, we see that ψ differs from unity by no more than 10% for $a_T \leq 500 \text{ km}$, meaning that we can safely set $\psi = 1$ for all the objects considered here. The classical Kuiper Belt is well represented by an annulus with inner and outer radii $R_i = 30AU$, $R_o = 50AU$, respectively, and thickness $H = 10AU$, for which the volume is $W = \pi H(R_o^2 - R_i^2) = 2 \times 10^{38} \text{ m}^3$. With these parameters and with $q = 4$, $a_{min} = 1 \text{ km}$ and $a_T = 50 \text{ km}$ we obtain $1/\tau \approx 10^{-2} \text{ Myr}^{-1}$ for objects in the classical Kuiper Belt. The rate increases with decreasing projectile size (for example, with $a_{min} = 0.1 \text{ km}$, the corresponding rate is $1/\tau \approx 10^1 \text{ Myr}^{-1}$), showing the importance of small impacts.

For the resurfacing model, we follow the prescription in Luu and Jewitt (1996). From Equations 5-7 and 9 of that paper, the ejecta blanket radius is found to be

$$r_{eb} = 17 \text{ km} (a/1 \text{ km})^{0.69} / (a_T/100 \text{ km})^{0.31}. \quad (10)$$

We again assume $q = 4.0$, noting that this index is determined for large KBOs ($a > 50 \text{ km}$) and may not hold for the smaller objects which dominate collisional resurfacing. We computed Monte Carlo simulations for 1 *Gyr* at a time resolution of 1 *Myr*, using a 1000 x 1000 pixel array to represent the surface. Other important parameters include the timescale for radiation damage of the surface, which we take to be 10^8 yrs (Luu and Jewitt 1996) and the minimum impactor size, for which we assumed a range of values $0.05 \leq a_{min} \leq 1.0 \text{ km}$. Sample models with $a_{min} = 0.05 \text{ km}$ are shown in Figure 12.

The principal features of the data that we seek to compare with the resurfacing simulations are 1) the wide spread in the surface colors and 2) the absence of a measurable color-diameter trend. As noted in Luu and Jewitt (1996), steeper projectile size distributions increase the weight given to numerous, small impacts relative to rare, global resurfacing events. For this reason, the stochastic character of the new simulations is smaller than in Luu and Jewitt 1996. In fact, the $q = 4$, $a_T = 50 \text{ km}$ models show much less scatter than

do the real KBOs (Figure 12). In the observational sample the standard deviation on the mean of 28 measurements is $\sigma(V - R) = 0.02$ mag (Table 4), corresponding to 0.11 mag. per object. The peak-to-peak color range in $V - R$ is 0.5 mag. (Figure 3). On the other hand, the resurfacing models typically give much more muted variations with peak-to-peak excursions < 0.1 mag. Our first conclusion is that the color dispersion observed among the KBOs is larger than given by our $q = 4$ resurfacing model.

The resurfacing simulations predict a color-diameter trend, caused by the size dependence of the impact resurfacing time relative to the (constant) timescale for cosmic ray irradiation damage of the surface (Figure 12). The small KBOs are rapidly and repeatedly resurfaced, preventing them from reddening under the effects of cosmic rays whereas the large KBOs are difficult to resurface and therefore more susceptible to cosmic ray irradiation. Small KBOs also display substantial color dispersion relative to the larger objects because the colors are less affected by spatial averaging. However, the color differences as a function of KBO size are modest. In the size domain of the observed objects, between $a_T = 50$ km and $a_T = 250$ km, the mean $V - R$ varies by only 0.1 mag. (Figure 12). A factor of 5 in radius corresponds, at constant albedo, to a 3.5 magnitude brightness difference. Inspection of the data shows that a 0.1/3.5 [mag./mag.] color-magnitude gradient is too small to be seen in the real KBO sample, in view of the large intrinsic scatter. We conclude that the absence of a color-diameter trend in the KBO sample does not by itself constitute evidence against the action of resurfacing.

Perhaps the least model-dependent and, therefore, most serious blow against the resurfacing hypothesis is its prediction that, for objects of a given diameter, azimuthal color variations should be equal in magnitude to the color dispersion among objects. That this is not the case among the real KBOs may be seen by inspection of Table 5. There, repeated determinations of the colors taken at random rotational phases are in general agreement

within the quoted uncertainties of measurement while color differences between the KBOs are many times larger. The most significant exception is 1996 TL₆₆. Even here, however, the $V - R$ color range of 0.24 ± 0.08 mag. is small compared to the 0.5 mag. peak-to-peak color differences between objects (Tables 2, 3). If resurfacing were the primary cause of the well-established color differences between KBOs, then rotational color variations from $V - R = 0.35$ to $V - R = 0.80$ would be seen in *individual* KBOs, and this is clearly not the case.

We conclude that impact resurfacing is probably not the primary cause of the color differences which exist among the KBOs. It remains possible that resurfacing plays a secondary role, and may be responsible for azimuthal spectral variations like those reported on Centaur (8405) Asbolus (Kern et al. 2000). As noted in Luu and Jewitt (1996), resurfacing produces a range of colors only if the timescales for impact resurfacing and cosmic ray reprocessing are of the same order. Neither timescale is easy to estimate. The irradiation timescale depends on the cross-section for interaction between the cosmic rays and the molecules comprising the KBO surface layers. This cross-section is highly composition dependent. The resurfacing timescale is dominated by the abundance of impactors which are too small to be detected in current surveys and whose statistics are therefore uncertain. Furthermore, impact gardening of KBO regoliths may be important in exposing previously buried material, as on the Moon, and modelling this effect introduces additional levels of arbitrariness. The net result is that we cannot argue, on physical grounds, that the relevant timescales are of the same order of magnitude, as is required for the hypothesis to succeed. Neither is it completely obvious that the color of an irradiated ice mixture changes with the fluence in the simple way assumed by the resurfacing hypothesis. Indeed, laboratory experiments show a more complicated relationship.

It is unlikely that simple grain size effects could be responsible for such a wide color

diversity (Moroz *etal.* 1998). Instead, real compositional variations seem to be responsible. In the main (Mars - Jupiter) asteroid belt, some colorimetric diversity is produced by impact shattering of internally differentiated precursor bodies. This is not likely to be the explanation in the Kuiper Belt, where the 100 km and larger objects studied here are too large to have been produced by fragmentation of precursors (Farinella and Davis 1996). As noted above, the compositional gradient in the main-belt caused by a strong impressed radial temperature gradient is also unlikely to be relevant in the Kuiper Belt, where temperatures are low and temperature differences are small. The primary origin of the color dispersion remains unknown.

3.1. Other Reported Correlations

Tegler and Romanishin (2000) reported that all 9 observed KBOs with perihelia $q > 40$ AU systematically belong to their "red" group, while objects with smaller q are distributed more evenly between the red and grey groups. They showed that the probability of finding this result by random selection from a bimodal distribution is about $1/512$, corresponding to about 3σ in a Gaussian error distribution and argued that the effect is therefore of probable statistical significance.

We have re-examined Tegler and Romanishin's 1998 and 2000 data without making the classification of objects into "red" and "grey", since the data provide no support for this division. We use the $B - R$ color index as our metric, as this is more robust relative to measurement errors than either $B - V$ or $V - R$ separately. In their combined sample of 32 objects having $B - R$ color indices, there are 26 with $q < 40$ AU, for which the median value $(B - R)_m = 1.54$. All 6 objects with $q > 40$ AU have $B - R > (B - R)_m$. Given that the probability of any measurement falling above the median is, by definition, $1/2$, the chance that all of 6 values would be larger than $(B - R)_m$ is $(1/2)^6 = 1/64$. The combined data

sets from TR98, TR00 and this paper (Table 2) include 45 different objects with measured $B - R$ indices. We averaged separate measurements of multiply observed objects to obtain one $B - R$ per object. The median color for the 36 objects with $q < 40$ AU is $(B - R)_m = 1.46$, while all 9 objects with $q > 40$ AU have $B - R > (B - R)_m$. If the $q > 40$ AU objects have the same median color as those with smaller perihelia, the probability of obtaining the observed result is $(1/2)^9 = 1/512$. We therefore concur with TR00 that there is statistical ($\approx 3\sigma$) evidence for a color difference between objects having perihelia on either side of the $q = 40$ AU boundary. Clearly, however, this remains a weak result that should be tested by substantially increasing the sample size, particularly for objects with $q > 40$ AU. Until this is done, we see little point in speculating about possible causes of the color difference.

Levison and Stern (2001) reported a size dependence of the inclination distribution of KBOs, such that objects with absolute magnitude, $H < 6.5$ have a wider inclination distribution than others. However, using the Kolmogorov-Smirnov test, they find a 3% probability that the measured $H < 6.5$ and $H > 6.5$ distributions are drawn from the same parent population, corresponding to a result with 97% confidence. This, in turn, corresponds to about 2.2σ in a Gaussian probability distribution and is therefore formally insignificant. Our own data show no evidence for a color - magnitude trend (Table 3), and no evidence that the $H < 6.5$ and $H > 6.5$ color distributions are different.

4. Near-Infrared Spectra

Near infrared spectral observations were obtained using the Keck I 10m and the Subaru 8-m telescopes. At Keck, we used the NIRC spectrometer (Matthews and Soifer 1994) at the $f/25$ forward Cassegrain focus. NIRC contains a 256×256 pixel InSb array with $30\mu\text{m}$ pixels and a corresponding image scale of 0.15 arcsec per pixel (38 arcsec FOV). A slit of projected dimensions $0.68 \text{ arcsec} \times 38 \text{ arcsec}$ was used in conjunction with 150 line/mm

and 120 line/mm gratings for the JH and HK spectral regions, respectively, giving spectral resolutions $\lambda/\Delta\lambda \approx 100$. Observations were taken in several steps. First, NIRC broadband images were used to identify the target KBOs by their motion relative to the fixed stars. Second, non-sidereal rates were entered into the telescope control system in order to follow the motion of the KBO. The telescope was moved while autoguiding to place the object at the slit location and the alignment was checked, iteratively, using further broadband images. Next, the slit and grism were inserted into the beam. A spectrum was taken while dithering the target image between two positions along the slit separated by 10 arcsec. The alignment was re-checked every 20 - 30 minutes by removing the slit and re-imaging the target. Spectral flat fields were obtained by imaging a diffusely illuminated spot inside the dome. Spectral calibration of the images was obtained from nearby stars on the UKIRT Faint Standards list (Hawarden *et al.* 2001). In addition, we observed nearby solar analogue stars in order to cancel features specific to the solar spectrum.

At the Subaru 8-meter telescope we employed the CISCO camera in spectroscopic mode to acquire separate spectra in the JH and HK windows. CISCO is a high-throughput grating-dispersed near infrared spectrometer using a 1024×1024 HgCdTe array of $18.5\mu\text{m}$ pixels as detector (Motohara *et al.* 1998). The pixel scale is 0.11 arcsec/pixel, giving a $110 \text{ arcsec} \times 110 \text{ arcsec}$ FOV. The spectral resolution was $\lambda/\Delta\lambda = 1000$. We identified the targets again through their proper motions. At the time of use, Subaru could not track at non-sidereal rates. For this reason, we observed 2000 EB₁₇₃ near its stationary point to minimise the angular motion. As precautions, we used a relatively wide (1.0 arcsec) slit and we aligned the slit parallel to the apparent proper motion vector so that the natural motion of the object would carry it along, rather than out of the slit. As with NIRC, the alignment was periodically checked using broadband images and corrected when necessary. Flat fields were created from medians of the data. Calibration was again obtained using stars from Hawarden *et al.* 2001. The parameters of the spectral observations are listed in Table 9.

Spectral data reduction included steps to create and apply a bad pixel mask, flattening of the data, subtraction of night sky lines using adjacent dithered image pairs, removal of night sky line residuals by interpolation through the object position and, finally, extraction of the object spectrum. Variability in the transmission of the atmosphere, particularly in the water bands near $1.9\mu\text{m}$, also limit the photometric accuracy in some of the data. Fortunately, most observations were taken in dry atmospheric conditions and it was possible to take useful data through the atmospheric water absorption band. Nevertheless, systematic errors due to night sky lines and variable atmospheric extinction rival or dominate statistical errors in the spectra from NIRC. The higher resolution of the Subaru CISCO spectra allowed more accurate subtraction of the night sky lines. The signal per resolution element in the CISCO data is very small, however, so that we must bin the data to obtain useful spectral information.

The reduced spectra are shown in Figs. 13-17, where they have been divided by the spectrum of the Sun and normalized to unity at $2.2\mu\text{m}$. In Table 10 we list the normalized reflectivities binned to $0.1\mu\text{m}$ resolution. Error bars on the binned points are 1σ standard deviations on the means of the pixels within each bin. For each spectrum in Figs. 13-17 we show the individual data points and overplot the binned data. We have included the spectrum of 1996 TL₆₆ from Luu and Jewitt (1998) for comparison with the new data. It was obtained at the Keck telescope using NIRC and observing procedures identical to those employed for the other KBOs.

4.1. 2000 EB₁₇₃

Meaningful interpretation of the spectra demands a full understanding of systematic effects due to imperfect atmospheric extinction and sky line cancellation. These are best estimated empirically, by comparing spectra of standard stars taken at different times and

airmasses. The cleanest case is 2000 EB₁₇₃ (Fig. 13), for which the night was dry and stable and the 1.9 μ m telluric absorption feature is correspondingly well cancelled. The binned data suggest a broad absorption band centered near 2.0 μ m but, in view of the likely systematic uncertainties, we do not claim this feature as significant. We agree with Brown *et al.* (2000), that the spectrum of 2000 EB₁₇₃ is featureless in the $1.0 \leq \lambda \leq 2.5\mu$ m wavelength range. Unique compositional diagnoses of featureless spectra are obviously impossible. It is interesting to note, however, that laboratory reflection spectra of highly carbonized materials are commonly neutral and featureless, reflecting a deficiency of hydrogen bonds (Cloutis *et al.* 1994, Moroz *et al.* 1998). In the KBOs, we expect that hydrogen will be mobilized in the surface layers by continued cosmic ray bombardment, leading to eventual escape and a net hydrogen depletion regardless of the initial composition.

4.2. 1999 DE₉

In contrast, 1999 DE₉ is spectrally structured (Fig. 14). Absorption features are evident near 1.4 μ m, 1.6 μ m, 2.00 μ m and (possibly) at 2.25 μ m. The continuum drops from 1.3 μ m down to the limit of the spectrum at 1.0 μ m, which we interpret as an additional broad absorption centered at or shortward of 1.0 μ m. Water ice has well-known features at 1.55 μ m, 1.65 μ m, and 2.02 μ m. The 1.55 μ m and 1.65 μ m features appear very weakly in the DE₉ spectrum; we note this is a characteristic of spectra of fine grain frost (Clark 1981a). Water ice also has a high-overtone band at 1.25 μ m, which is not seen in the DE₉ spectrum. The suppression of high-overtone bands relative to the low-overtones (bands at longer wavelengths) is observed when other minerals are present in addition to water ice (Clark 1981a), and this might explain the absence of the 1.25 μ m feature in 1999 DE₉. The strongest water band at 2.00 μ m is only about 10% deep. The general weakness of the water ice features suggests a low abundance of water ice, or water ice that is heavily contaminated

by an absorbing component. Indeed, the 1999 DE₉ spectrum is very similar to that of a mixture of Mauna Kea red cinder and 1% (by mass) water ice (Clark 1981b), shown in Figure 18. Notice that the $\approx 1.6\mu\text{m}$ features in the cinder spectrum are extremely weak, as in 1999 DE₉, and that the $\approx 2.0\mu\text{m}$ bands in the KBO and the Mauna Kea sample match in both position and width.

Features near $1.4\mu\text{m}$ and $2.25\mu\text{m}$ are usually diagnostic of the presence of metal-OH combination and overtone vibrational motions in minerals that incorporate OH within their crystal structure (Hunt 1977). The Mauna Kea spectrum in Figure 18 shows absorption near $1.4\mu\text{m}$ and a possible band at $2.22 - 2.25\mu\text{m}$. The exact location of these bands can be diagnostic of the compound (either Al or Mg) associated with the OH stretch, but the quality of the DE₉ spectrum is not good enough for us to make this identification. Given the limited spectral coverage and the unknown albedo, we tentatively assert that the spectrum of 1999 DE₉ shows evidence for the hydroxyl group, with the latter interacting with an Al- or Mg-compound. If it can be confirmed, the metal-hydroxyl identification would be most significant because the reactions that create the metal-OH compounds proceed only in the presence of liquid water, implying that temperatures near the melting point have been sustained in 1999 DE₉ for at least a short period of time. Localised impacts on surface materials on 1999 DE₉ might provide a sufficient (although transient) heat source. Heating of core volatiles by the prolonged decay of radioactive elements could also lead to melting but a mechanism of transport to the surface would in addition be required for these materials to be spectrally observable.

A similar absorption near $2.27\mu\text{m}$ is present in the spectrum of Centaur (5145) Pholus (Davies, Sykes and Cruikshank 1993, Luu, Jewitt and Cloutis 1994), with which 1999 DE₉ shares a resemblance in the $1.4 < \lambda < 2.4\mu\text{m}$ wavelength range (Figure 19). This feature has been tentatively interpreted as due to solid methanol (CH_3OH ; Cruikshank *et*

al. 1998). However, as Cruikshank *et al.* note, the identification with methanol is uncertain in part because an expected second band at $2.33\mu\text{m}$ is not observed. The Pholus spectrum modelled by these authors has an unfortunate gap at $1.4\mu\text{m}$. We recommend that this wavelength be observed to search for evidence for the counterpart metal-OH absorption feature suspected in 1999 DE₉.

Lastly, our spectrum of 1999 DE₉ shows a broad absorption in the $1.0 < \lambda < 1.3 \mu\text{m}$ wavelength region with an apparent minimum near $1.05\mu\text{m}$. Unfortunately, the minimum is close to the short wavelength end of our spectrum and we cannot be confident of the trend of the reflectivity at $\lambda \leq 1.0\mu\text{m}$. A true minimum near this wavelength would be suggestive of the presence of a ferrous silicate, possibly an olivine (Cloutis and Gaffey 1991). Forsterite (Mg_2SiO_4 , a magnesium rich olivine) has been independently proposed to fit a $1\mu\text{m}$ absorption in the reflection spectrum of Centaur (5145) Pholus (Cruikshank *et al.* 1998) and would fit the $1\mu\text{m}$ absorption in 1999 DE₉. The identification of Forsterite as the specific form of silicate is non-unique but it is attractive because of the known presence of Forsterite in the dust ejected from comets (Crovisier *et al.* 2000). The single object 1999 DE₉ thus provides plausible compositional ties to both the Centaurs and the nuclei of comets (which are known to be water rich) through the water ice (Foster *et al.* 1999, McBride *et al.* 1999, Luu, Jewitt and Trujillo 2000) and silicate (Cruikshank *et al.* 1998) bands. On the other hand, if the reflectivity continues to decline at $\lambda \leq 1.0\mu\text{m}$, we would instead suspect that the absorption is due to the same complex hydrocarbons (e.g. Tholins) that give reddish optical colors to the KBOs. Only new spectra will allow us to decide between these interpretations.

4.3. 1993 SC

Numerous absorptions were reported in the near infrared spectrum of 1993 SC by Brown *et al.* (1997). Their spectrum was taken at Keck with the NIRC spectrometer over a range of airmasses from 1.2 to 1.7 and with an integration time of 3600 seconds. They reported absorption features at $1.62\mu\text{m}$, $1.79\mu\text{m}$, $1.95\mu\text{m}$, $2.20\mu\text{m}$ and $2.32\mu\text{m}$, with depths up to 50% of the local continuum. The features were not precisely identified by Brown *et al.*, but a broad classification as hydrocarbon absorptions was made. We targetted the H-K spectral region of 1993 SC specifically to examine the features reported by Brown *et al.* Our integration of 6000 seconds was recorded between airmasses 1.04 and 1.09, with sky cancellation using a nearby star observed at airmass 1.08.

None of the features reported by Brown *et al.* are apparent in our data. Instead, using the same instrument on the same telescope but with a longer integration time, we find only a noisy continuum devoid of significant spectral structure (Fig. 16). In our spectrum, the reflectivity in the $2.25\mu\text{m} - 2.35\mu\text{m}$ bin is 1.01 ± 0.15 . This is incompatible with Brown *et al.*'s deepest minimum at $2.32\mu\text{m}$ at the 3.3σ level. (Brown *et al.* presented their data heavily smoothed by convolution with a Gaussian, which impedes a more detailed comparison with the unsmoothed data in Fig. 16). Simple experiments in which our data were smoothed by convolution with a Gaussian generated (apparently deep but unreal) features with wavelengths that did not match those reported by Brown *et al.* As another metric of comparison, we compute, $S_{2.2}/S_{1.6}$, the ratio of the reflectivity at K band ($S_{2.2}$) to that at H band ($S_{1.6}$). In the Brown *et al.* spectrum this ratio is $S_{2.2}/S_{1.6} = 2.2$ (see their Fig. 1), while we measure $S_{2.2}/S_{1.6} = 1.0 \pm 0.1$ (Fig. 16). Finally, earlier broadband photometry gives $\text{H-K} = -0.04 \pm 0.19$ (Jewitt and Luu 1998) which, with the solar $\text{H-K} = 0.06$, corresponds to $S_{2.2}/S_{1.6} = 0.91 \pm 0.19$. The filter photometry and our new spectrum are mutually consistent, but do not support the much larger $S_{2.2}/S_{1.6}$ of Brown *et al.* We

have no explanation for the differences between our spectrum and that of Brown *et al.*

4.4. Discussion

We also obtained spectra of 1996 TL₆₆ (Fig. 17, taken from Luu and Jewitt 1998), and 1996 TS₆₆ (Fig. 15). When considered with the spectrum of 1996 TO₆₆ (Brown, Cruikshank and Pendleton 1999) we see a remarkable diversity of spectral characteristics among the KBOs. Some (2000 EB₁₇₃, 1996 TL₆₆, 1996 TS₆₆ and 1993 SC) appear spectrally bland at the achievable signal-to-noise ratios. Others (1996 TO₆₆, 1999 DE₉) show absorptions due to water ice. The remarkable 1999 DE₉ shows additional evidence for absorption near 1 μ m that may indicate surface olivines and weaker bands as discussed above.

What do these spectral differences mean? There is no obvious correlation with the optical colors (e.g. $B - I$, Table 2) or absolute magnitudes. Indeed, it is too early to detect patterns in the spectral properties of the bodies in the outer solar system. An enlarged sample of high quality spectra is needed, which will require long integrations on the brightest KBOs with the largest telescopes. Parallel measurements of the albedos using simultaneous optical and thermal measurements (presumably from the SIRTf spacecraft but perhaps also from ground-based submillimeter telescopes) are also needed to better understand the compositions of the KBOs.

The Centaurs and the nuclei of the Jupiter-family comets probably share a common origin in the Kuiper Belt. Spectral observations of these objects should show a diversity parallel to that seen among the KBOs. Indeed, near infrared spectra of the Centaurs (2060) Chiron and (5145) Pholus show, respectively, neutral near infrared continuum with superimposed water ice bands but no other features (Foster *et al.* 1999, Luu, Jewitt and Trujillo 2000) and a structured continuum with evidence for olivine, a low mass hydrocarbon

(possibly methanol) as well as water (Cruikshank *et al.* 1999). Qualitatively, at least, these two Centaurs are analogues of Kuiper Belt Objects 1996 TO₆₆ (Brown, Cruikshank and Pendleton 1999) and 1999 DE₉ (Figure 14), respectively. Spectra of more Centaurs are urgently needed. Recent estimates predict that 20 - 30 Centaurs should have $m_R < 20$ and thus be within range of spectral investigation with the largest telescopes (Figure 4 of Sheppard *et al.* 2000). The nuclei of comets present an even more difficult observational challenge. They are small and tend to be surrounded by dust comae when close to the Sun and bright enough to be studied. Despite this, obtaining nucleus spectra should be a high scientific priority for those interested in the origin of the comets and the nature of the Kuiper Belt.

5. Summary

We present new optical photometry and near-infrared spectra of Kuiper Belt Objects, taken to study the spectral diversity among these bodies and to search for physically revealing correlations. We find that

1. The optical (B-V, V-R and R-I) and optical to near-infrared (V-J) colors of KBOs show a dispersion that is large compared to the uncertainties of measurement. The color indices are mutually correlated, indicating the ubiquitous presence of a single reddening agent in the $0.45\mu\text{m}$ to $1.2\mu\text{m}$ wavelength range.
2. There is no statistically significant (3σ) evidence for a bimodal distribution of the B-V vs. V-R colors, either in our sample or in the observations reported by Tegler and Romanishin (1998, 2000).
3. The colors are not linearly correlated with any orbital or known physical properties of the KBOs. Specifically, we find no linear correlation of the optical color indices

with heliocentric distance, orbital semi-major axis, inclination, eccentricity, circular velocity difference or absolute magnitude. However, at the 3σ confidence level, we do confirm Tegler and Romanishin’s (2000) finding that objects with perihelia $q > 40$ AU are systematically redder than others. The mean colors of the classical and resonant Kuiper Belt Objects are indistinguishable.

4. Impact resurfacing (Luu and Jewitt 1996) is probably not the primary cause of the color dispersion among KBOs, for two reasons. First, the color dispersion among KBOs is larger than can be easily produced in Monte Carlo models of the resurfacing process. Second, the resurfacing hypothesis predicts that, in a statistical sense, individual objects should show azimuthal color variations as large as the color differences between objects. The measurements show that this is not the case.
5. The KBOs are also spectrally diverse in the near-infrared, from featureless to continua marked by distinct solid state absorptions. In particular, 1999 DE₉ shows remarkable similarity to the spectrum of a Mauna Kea cinder plus water ice mixture, with a water ice feature near $2.0 \mu\text{m}$ and depression of the continuum at $\lambda \leq 1.3 \mu\text{m}$ that is consistent with (but not uniquely diagnostic of) olivine absorption.
6. Our $1.4 \mu\text{m} - 2.4 \mu\text{m}$ reflection spectrum of 1993 SC shows no evidence of the existence of absorption features reported by Brown *et al.* (1997). Furthermore, the spectral slope reported by Brown *et al.* is inconsistent with the spectral slope measured here, and with independent broadband photometry.

Acknowledgements

We thank Wayne Wack, Gary Punawai and John Dvorak for their observing assistance, and Support Scientists Ken Motohara and Bob Goodrich for their help with the set-ups. Chad Trujillo and Scott Sheppard helped with some of the observations. Ted Roush and

Ed Cloutis gave helpful comments on our spectrum of 1999 DE₉. John Davies provided a prompt review. We thank Jan Kleyna and Jing Li for discussions about statistics and we gratefully acknowledge support from NASA's Origins Program.

REFERENCES

- Barucci, M. A., Romon, J., Doressoundiram, A., and Tholen, D. (2000). *Astron. J.*, 120, 496-500.
- Barucci, M. A., Fulchignoni, M., Birlan, M., Doressoundiram, A., Romon, J., and Boehnhardt, H. (2001). *Astron. Ap.*, 371, 1150-1154.
- Brown, R., Cruikshank, D., Pendleton, Y. and Veeder, G. (1997). *Science*, 276, 973-939.
- Brown, R., Cruikshank, D., and Pendleton, Y. (1999). *Ap. J. Lett.*, 519, 101-104.
- Brown, M., Blake, G., and Kessler, J. (2000). *Ap. J. Lett.*, 543, 163-165.
- Clark, R. N. (1981a). *J. Geo. Res.* 86, 3087-3096.
- Clark, R. N. (1981b). *J. Geo. Res.* 86, 3074-3086.
- Cloutis, E. and Gaffey, M. J. (1991). *J. Geophys. Res.*, 96, 22809-22826.
- Cloutis, E., Gaffey, M., and Moslow, T. (1994). *Icarus*, 107, 276-287.
- Crovisier, J. *et al.* 2000. In *Thermal Emission Spectroscopy and Analysis of Dust, Disks and Regoliths*. eds. M. Sitko, A. Sprague and D. Lynch. ASP Conference Series, 196, 109-117.
- Cruikshank, D. *et al.* (1998). *Icarus*, 135, 389.
- Davies, J. K., Sykes, M. and Cruikshank, D. (1993). *Icarus*, 102, 166-169.
- Davies, J. K., McBride, N., and Green, S. F. (1997). *Icarus*, 125, 61-66.
- Davies, J. K., Green, S., McBride, N., Muzzerall, E., Tholen, D. J., Whiteley, R. J., Foster, M. J., and Hillier, J. K. (2000). *Icarus*, 146, 253-262.
- Ferrin, I. *et al.* (2001). *Ap. J. Lett.*, 548, 243-247.
- Farinella, P., and Davis, D. R. (1996). *Science*, 273, 938-941.
- Foster, M., Green, S., McBride, N., and Davies, J. (1999). *Icarus*, 141, 408.

- Green, S., McBride, O’Ceallaigh, D., Fitzsimmons, A., Williams, I. and Irwin, M. (1997).
Mon. Not. R. Astron. Soc., 290, 186-192.
- Hainaut, O., Delahodde, C., Boehnhardt, H., Dotto, E., Barucci, M., Meech, K., Bauer, J.,
West, R., and Doressoundiram, A. (2000). Astron. Ap., 356, 1076-1088.
- Hartigan, J.A. and Hartigan, P.M. (1985), Annals of Statistics, 13, 70-84.
- Hartmann, W., Cruikshank, D., and Degewij, J. (1982). Icarus, 52, 377.
- Hartmann, W., Tholen, D., Meech, K., and Cruikshank, D. (1990). Icarus, 83, 1.
- Hawarden, T., Leggett, S. K., Letawsky, M., Ballantyne, D., and Casali, M. (2001). Mon.
Not. R. Astron. Soc., 325, 563
- Hunt, G. R. (1977). Geophysics, 42, 501-513.
- Jewitt, D. C., Luu, J., and Chen, J. (1996). Astron. J., 112, 1225.
- Jewitt, D. C., and Luu, J. X. (1998). Astron. J., 115, 1667-1670.
- Jewitt, D. C., Luu, J., and Trujillo, C. (1998). Astron. J., 115, 2125-2135.
- Jones, J., Christian, C., and Waddell, P. (1988). Pub. Astr. Soc. Pas., 100, 489-495.
- Kern, S., McCarthy, D., Buie, M., Brown, R., Campins, H., and Rieke, M. (2000). Ap. J.
Lett., 542, 155-159.
- Landolt, A. 1992. A. J., 104, 340 - 371.
- Levison, H., and Stern, S. A. (2001). Astron. J., 121, 1730-1735.
- Luu, J. X., Jewitt, D. C. and Cloutis, E. (1994). Icarus, 109, 133-144.
- Luu, J. X., and Jewitt, D. C. (1996). Astron. J., 112, 2310-2318.
- Luu, J., Marsden, B., Jewitt, D., Trujillo, Hergenrother, C., Chen, J. and Offutt, W. (1997).
Nature, 387, 573.
- Luu, J. X., and Jewitt, D. C. (1998). Ap. J. Lett., 494, 117-121.

- Luu, J. X., Jewitt, D. C. and Trujillo (2000). *Ap. J. Lett.*, 531, 151-154
- Matthews, K., and Soifer, B. T. (1994). In *Infrared Astronomy with Arrays*, ed. I. McLean, Kluwer, Dordrecht. p. 239-246.
- McBride, N., Davies, J., Green, S., and Foster, M. (1999). *Mon. Not. Royal. Astr. Soc.*, 306, 799-805.
- Moroz, L., Arnold, G., Korochantsev, A., and Wasch, R. (1998). *Icarus*, 134, 253-268.
- Motohara, K., Maihara, T., Iwamuro, F., Oya, S., Imanishi, M., Terada, H., Goto, M., Iwai, J., Tanabe, H., Tsukamoto, H., and Sekiguchi, K. (1998). *Proc. SPIE*, 3354, “Infrared Astronomical Instrumentation,” Albert M. Fowler, Ed., p. 659-667.
- Noll, K. S., Luu, J., and Gilmore, D. (2000). *Astron. J.*, 119, 970-976.
- Oke, J., Cohen, J., Carr, M., Cromer, J., Dingizian, A., Harris, F., Labrecque, S., Lucinio, R., Schaal, W., Epps, H., and Miller, J. (1995). *P. A. S. P.*, 107, 375.
- Sheppard, S., Jewitt, D., Trujillo, C., Brown, M., and Ashley, M. (2000). *Astron. J.*, 120, 2687-2694.
- Tegler, S. C., and Romanishin, W. (1998). *Nature*, 392, 49-50.
- Tegler, S. C., and Romanishin, W. (2000). *Nature*, 407, 979-981.
- Trujillo, C., Jewitt, D., and Luu, J. (2000). *Ap. J. Lett.*, 529, 103-106.
- Trujillo, C., Jewitt, D., and Luu, J. (2001). *Astron. J.*, 122, 457-473.
- Weintraub, D., Tegler, S., and Romanishin, W. (1997). *Icarus*, 128, 456-463.

Figure Captions

Figure 1. Keck image of 1996 SZ₄ (circled) with a grid of artificial images added to assess the noise properties of the data. The magnitudes of the synthesized images vary vertically in the figure, as marked. At each magnitude, seven artificial images have been added to measure the effect of background fluctuations on the extracted photometry. This is a 300 second integration through the R filter, taken 1998 November 14.

Figure 2. Sample photometric uncertainties as a function of apparent magnitude in the BVR and I filters for 300 sec integrations, measured from simulations like the one in Figure 1. The curves show Eq. (4) fitted to the data.

Figure 3. Plot of B-V vs. V-R for photometry from the present work having $\sigma_{B-V} < 0.15$ (see Table 2). The color of the Sun is marked. The least squares fit is shown to guide the eye.

Figure 4. Plot of V-R vs. R-I for photometry from the present work having $\sigma_{B-V} < 0.15$ (see Table 2). The color of the Sun is marked.

Figure 5. Plot of B-V vs. B-I for photometry from the present work having $\sigma_{B-V} < 0.15$ (see Table 2). The color of the Sun is marked.

Figure 6. Plot of B-I vs. V-J for KBOs observed independently in the near-infrared by Jewitt and Luu (1998) and Davies *et al.* 2000.

Figure 7. Comparison of the V-R colors of KBOs measured in this work and reported independently. TR98, TR00 are Tegler and Romanishin 1998 and 2000, respectively, JL98 is Jewitt and Luu 1998 while B00 is Barucci *et al.* 2000. The solid line is the track expected if the measurements are equal. Error bars have been suppressed for clarity: they may be read from Table 5.

Figure 8. B-V vs. V-R from Tegler and Romanishin (1998).

Figure 9. B-V vs. V-R from Tegler and Romanishin (2000).

Figure 10. Probability of obtaining a Largest Interval (LI) greater than the one observed in a random sampling of a uniform distribution in $B - V$. The probabilities were calculated as described in the text. Solid lines are marked with the number of data points included in each simulation. Dashed lines mark 2σ and 3σ statistical confidence levels. Points show the observational samples.

Figure 11. Same as Fig. 10 but for the $V - R$ color index.

Figure 12. Sample resurfacing models computed as described in section 3. The curves show simulated color evolution on three KBOs having radii $a_T = 5, 50$ and 250 km (bottom to top). A $q = 4$ size distribution is used, as suggested by the observations, with a minimum projectile radius $a_{min} = 0.05$ km. At the right we show the mean colors and the standard color deviations for each model.

Figure 13. Reflection spectrum of 2000 EB₁₇₃ taken with the Subaru telescope. The raw data are plotted in grey. The black circles denote the reflectivity binned to $0.1\mu\text{m}$ resolution (see also Table 10). The solid line is a linear, least squares fit to the data.

Figure 14. Reflection spectrum of 1999 DE₉ taken with the Keck telescope. The grey line shows the raw data. The black line through the data is a running mean added to guide the eye.

Figure 15. Reflection spectrum of 1996 TS66 taken with the Keck telescope. Individual pixels are plotted in grey. The black circles denote the reflectivity binned to $0.1\mu\text{m}$ resolution (see also Table 10).

Figure 16. Same as Figure 12 but for 1993 SC.

Figure 17. Same as Figure 12 but for 1996 TL66 (from Jewitt and Luu 1998).

Figure 18. Reflection spectrum of 1999 DE₉ compared with a Mauna Kea cinder plus 1% water ice (by weight) sample from Clark 1981b. The 1999 DE₉ spectrum is shown unsmoothed (grey line) and running-box smoothed by $0.05\mu\text{m}$ (black line). The Mauna Kea spectrum has been vertically offset for clarity.

Figure 19. Reflection spectrum of 1999 DE₉ compared with the spectrum of Centaur (5145) Pholus (from Luu, Jewitt and Cloutis 1994). The 1999 DE₉ spectrum is shown unsmoothed (grey line) and running-box smoothed by $0.05\mu\text{m}$ (black line). The (5145) Pholus spectrum has been vertically offset for clarity.

Table 1. Geometrical Circumstances of the Observations

Object	Class	Telescope	UT Date	R [AU]	D [AU]	α [deg]
Pluto	3:2	UH 2.2-m	2000 May 01	30.26	29.41	1.04
1992 QB ₁	CKBO	Keck 10-m	1998 Nov 14	40.91	40.19	0.96
1993 SB	3:2	Keck 10-m	1998 Nov 15	31.05	30.3	1.28
1993 SC	3:2	Keck 10-m	1998 Nov 14	34.66	33.94	1.14
1994 TA	Centaur	Keck 10-m	1998 Nov 14	16.93	15.96	0.74
1994 TB	3:2	Keck 10-m	1998 Nov 15	30.08	29.48	1.51
1995 DA ₂	4:3	Keck 10-m	1998 Nov 14	34.06	33.95	1.65
1995 WY ₂	CKBO	Keck 10-m	1998 Nov 15	47.42	46.56	0.58
1995 WY ₂	CKBO	Keck 10-m	1998 Nov 14	47.42	46.57	0.60
1996 RQ ₂₀	CKBO	Keck 10-m	1998 Nov 15	39.46	38.70	0.91
1996 RR ₂₀	3:2	Keck 10-m	1998 Nov 14	43.55	43.17	1.20
1996 SZ ₄	3:2	Keck 10-m	1998 Nov 14	30.24	29.45	1.14
1996 TK ₆₆	CKBO	Keck 10-m	1998 Nov 15	42.84	42.16	0.96
1996 TL ₆₆	SKBO	Keck 10-m	1998 Nov 14	35.09	34.14	0.43
1996 TO ₆₆	CKBO	Keck 10-m	1998 Nov 14	45.86	45.25	0.97
1996 TP ₆₆	3:2	Keck 10-m	1998 Nov 14	26.39	25.49	0.93
1996 TQ ₆₆	3:2	Keck 10-m	1998 Nov 15	34.61	33.70	0.65
1996 TS ₆₆	CKBO	Keck 10-m	1998 Nov 15	38.82	37.87	0.37
1997 CQ ₂₉	CKBO	Keck 10-m	1998 Nov 15	41.28	41.57	1.30
1997 CR ₂₉	2:1?	Keck 10-m	1998 Nov 15	41.85	41.76	1.35
1997 CS ₂₉	CKBO	Keck 10-m	1998 Nov 14	43.6	43.17	1.17
1997 CU ₂₆	Centaur	Keck 10-m	1998 Nov 15	13.55	13.54	4.18
1997 CU ₂₉	CKBO	Keck 10-m	1998 Nov 15	44.75	44.29	1.12
1997 QH ₄	CKBO	Keck 10-m	1998 Nov 15	41.41	40.86	1.14

Table 1—Continued

Object	Class	Telescope	UT Date	R [AU]	D [AU]	α [deg]
1997 QJ ₄	3:2	Keck 10-m	1998 Nov 15	34.72	34.16	1.35
1998 SN ₁₆₅	CKBO	Keck 10-m	1998 Nov 14	38.24	37.75	1.23
1999 DE ₉	SKBO	UH 2.2-m	2000 Apr 28	33.81	33.78	1.54
1999 KR ₁₆	CKBO	UH 2.2-m	2000 Apr 28	38.05	37.07	0.34
2000 EB ₁₇₃	3:2	UH 2.2-m	2000 Jul 01	29.87	29.73	1.93

Table 2. Optical Photometry

Object	Date	$m_R(1, 1, 0)$	R	B-V	V-R	R-I
		[mag]	[mag]	[mag]	[mag]	[mag]
Pluto	2000 May 01	-1.37	13.42 ± 0.01	0.86 ± 0.01	0.48 ± 0.01	0.40 ± 0.01
1992 QB ₁	1998 Nov 14	6.98	23.10 ± 0.09	0.99 ± 0.18	0.66 ± 0.15	0.80 ± 0.15
1993 SB	1998 Nov 15	7.91	22.83 ± 0.07	0.78 ± 0.12	0.51 ± 0.11	0.49 ± 0.15
1993 SC	1998 Nov 14	6.73	22.13 ± 0.04	1.05 ± 0.10	0.80 ± 0.07	0.75 ± 0.07
1994 TA	1998 Nov 14	11.25	23.44 ± 0.12	1.36 ± 0.29	0.62 ± 0.20	0.74 ± 0.21
1994 TB	1998 Nov 15	7.55	22.35 ± 0.05	1.19 ± 0.11	0.71 ± 0.08	0.77 ± 0.08
1995 DA ₂	1998 Nov 14	8.13	23.51 ± 0.13	1.31 ± 0.27	0.51 ± 0.20	0.63 ± 0.24
1995 WY ₂	1998 Nov 15	6.88	23.62 ± 0.14	1.03 ± 0.28	0.60 ± 0.23	0.51 ± 0.28
1995 WY ₂	1998 Nov 14	6.95	23.69 ± 0.15	–	–	–
1996 RQ ₂₀	1998 Nov 15	6.78	22.74 ± 0.07	0.96 ± 0.13	0.58 ± 0.11	0.71 ± 0.12
1996 RR ₂₀	1998 Nov 14	6.72	23.14 ± 0.10	1.10 ± 0.21	0.69 ± 0.16	0.76 ± 0.16
1996 SZ ₄	1998 Nov 14	8.34	23.13 ± 0.10	0.55 ± 0.15	0.61 ± 0.15	0.62 ± 0.17
1996 TK ₆₆	1998 Nov 15	6.30	22.62 ± 0.06	1.08 ± 0.13	0.69 ± 0.10	0.59 ± 0.12
1996 TL ₆₆	1998 Nov 14	5.04	20.45 ± 0.02	0.72 ± 0.03	0.38 ± 0.03	0.35 ± 0.03
1996 TO ₆₆	1998 Nov 14	4.49	21.11 ± 0.03	0.72 ± 0.03	0.40 ± 0.04	0.39 ± 0.04
1996 TP ₆₆	1998 Nov 14	6.85	21.03 ± 0.02	1.13 ± 0.04	0.69 ± 0.04	0.72 ± 0.04
1996 TQ ₆₆	1998 Nov 15	7.17	22.53 ± 0.06	1.22 ± 0.13	0.69 ± 0.10	0.75 ± 0.10
1996 TS ₆₆	1998 Nov 15	5.86	21.71 ± 0.03	1.10 ± 0.06	0.69 ± 0.05	0.62 ± 0.06
1997 CQ ₂₉	1998 Nov 15	6.50	22.72 ± 0.07	0.99 ± 0.13	0.64 ± 0.11	0.57 ± 0.13
1997 CR ₂₉	1998 Nov 15	7.04	23.31 ± 0.11	0.67 ± 0.20	0.69 ± 0.18	0.51 ± 0.22
1997 CS ₂₉	1998 Nov 14	5.11	21.53 ± 0.03	1.16 ± 0.06	0.61 ± 0.05	0.66 ± 0.05
1997 CU ₂₆	1998 Nov 15	6.39	17.87 ± 0.02	0.84 ± 0.03	0.50 ± 0.03	0.52 ± 0.03
1997 CU ₂₉	1998 Nov 15	6.22	22.75 ± 0.07	1.12 ± 0.14	0.59 ± 0.11	0.58 ± 0.13
1997 QH ₄	1998 Nov 15	6.88	23.07 ± 0.09	1.05 ± 0.18	0.65 ± 0.15	0.64 ± 0.16

Table 2—Continued

Object	Date	$m_R(1, 1, 0)$ [mag]	R [mag]	B-V [mag]	V-R [mag]	R-I [mag]
1997 QJ ₄	1998 Nov 15	7.31	22.73 ± 0.07	0.70 ± 0.12	0.63 ± 0.11	0.31 ± 0.15
1998 SN ₁₆₅	1998 Nov 14	5.37	21.22 ± 0.03	0.71 ± 0.04	0.40 ± 0.04	0.40 ± 0.05
1999 DE ₉	2000 Apr 28	4.68	20.04 ± 0.02	0.94 ± 0.03	0.57 ± 0.03	0.56 ± 0.03
1999 KR ₁₆	2000 Apr 28	5.49	21.25 ± 0.02	1.10 ± 0.05	0.74 ± 0.03	0.77 ± 0.03
2000 EB ₁₇₃	2000 Jul 01	4.61	19.43 ± 0.02	0.93 ± 0.04	0.65 ± 0.03	0.59 ± 0.03

Table 3. Correlations

Quantity ¹	Quantity ¹	N^2	r_{corr} ³	$P(r \geq r_{corr})^4$
B-I	V-J	10	0.97	< 0.001
B-V	R-I	28	0.70	< 0.001
V-R	R-I	28	0.71	< 0.001
B-V	V-R	27	0.44	0.02
B-I	$m_R(1, 1, 0)$	28	0.38	0.05
B-I	a	28	0.21	> 0.1
B-I	e	28	0.30	> 0.1
B-I	i	28	-0.08	> 0.1
B-I	m_R	28	0.35	0.05
B-I	q	28	0.18	> 0.1
B-I	R_h	28	0.02	> 0.1
B-I	ΔV	28	0.19	> 0.1

¹ $m_R(1, 1, 0)$ = red magnitude reduced to $R = \Delta = 1AU$ and to phase angle $\alpha = 0$ deg. a = semi-major axis, q = perihelion distance, R_h = heliocentric distance, ΔV = velocity relative to uninclined, circular Keplerian orbit

²Number of measurements in the sample

³Linear correlation coefficient

⁴Probability that a larger correlation coefficient could be obtained by chance from N measurements of uncorrelated data. $P < 0.003$ indicates a correlation with $> 3\sigma$ significance.

Table 4. Color Means

Sample ¹	N^2	$B - V^3$	$V - R^3$	$R - I^3$	$B - I^3$
Classical	12	1.00 ± 0.04	0.61 ± 0.03	0.60 ± 0.04	2.22 ± 0.10
All Resonant	12	0.96 ± 0.07	0.64 ± 0.03	0.61 ± 0.04	2.20 ± 0.12
3:2 Only	10	0.95 ± 0.07	0.65 ± 0.03	0.62 ± 0.05	2.21 ± 0.14
All	28	0.98 ± 0.04	0.61 ± 0.02	0.60 ± 0.03	2.18 ± 0.07

¹Dynamical sub-sample.

²Number of measurements in the sub-sample

³Mean color and standard deviation on the mean.

Table 5. Comparison of Optical Measurements

Object	Source	$m_R(1, 1, 0)$ [mag]	B-V [mag]	V-R [mag]	R-I [mag]
1992 QB ₁	(This work)	6.98 ± 0.09	0.99 ± 0.18	0.66 ± 0.15	0.80 ± 0.15
	(TR00)	6.92 ± 0.05	0.92 ± 0.06	0.78 ± 0.03	–
1993 SB	(This work)	7.91 ± 0.07	0.78 ± 0.12	0.51 ± 0.11	0.49 ± 0.15
	(TR00)	7.80 ± 0.04	0.82 ± 0.03	0.47 ± 0.04	–
1993 SC	(This work)	6.73 ± 0.04	1.05 ± 0.09	0.80 ± 0.07	0.75 ± 0.07
	(LJ96)	6.56 ± 0.05	0.92 ± 0.11	0.57 ± 0.09	0.86 ± 0.10
	DMG97	6.49 ± 0.10	–	0.54 ± 0.14	0.43 ± 0.14
	(JL98)	6.71 ± 0.02	0.94 ± 0.06	0.68 ± 0.05	0.68 ± 0.04
	(TR98)	–	1.27 ± 0.11	0.70 ± 0.04	–
1994 TB	(This work)	7.55 ± 0.05	1.19 ± 0.11	0.71 ± 0.08	0.77 ± 0.08
	(TR98)	–	1.10 ± 0.15	0.68 ± 0.06	–
1996 CU ₂₆	(This work)	6.39 ± 0.02	0.84 ± 0.03	0.50 ± 0.03	0.52 ± 0.03
	(TR98)	–	0.77 ± 0.05	0.48 ± 0.01	–
	(M99)	6.18 ± 0.05	–	0.46 ± 0.02	0.56 ± 0.03
1996 RQ ₂₀	(This work)	6.78 ± 0.07	0.96 ± 0.13	0.58 ± 0.11	0.71 ± 0.12
	(TR98)	–	–	0.44 ± 0.05	–
1996 RR ₂₀	(This work)	6.72 ± 0.10	1.10 ± 0.21	0.69 ± 0.16	0.76 ± 0.16
	(TR00)	6.51 ± 0.03	1.16 ± 0.04	0.71 ± 0.03	–
1996 SZ ₄	(This work)	8.34 ± 0.10	0.55 ± 0.15	0.61 ± 0.15	0.62 ± 0.17
	(TR00)	8.04 ± 0.04	0.83 ± 0.03	0.52 ± 0.02	–
1996 TK ₆₆	(This work)	6.30 ± 0.06	1.08 ± 0.13	0.69 ± 0.10	0.59 ± 0.12
	(TR00)	6.21 ± 0.04	0.99 ± 0.02	0.63 ± 0.02	–
1996 TL ₆₆	(This work)	5.04 ± 0.02	0.72 ± 0.03	0.37 ± 0.03	0.36 ± 0.04
	(JL98)	5.32 ± 0.04	0.58 ± 0.05	0.13 ± 0.07	0.54 ± 0.04

Table 5—Continued

Object	Source	$m_R(1, 1, 0)$ [mag]	B-V [mag]	V-R [mag]	R-I [mag]
	(TR98)	–	0.75 ± 0.02	0.35 ± 0.01	–
1996 TO ₆₆	(This work)	4.49 ± 0.03	0.72 ± 0.04	0.40 ± 0.04	0.39 ± 0.04
	(JL98)	4.52 ± 0.05	0.59 ± 0.06	0.32 ± 0.06	0.36 ± 0.07
	(TR98)	–	0.74 ± 0.04	0.38 ± 0.03	–
1996 TP ₆₆	(This work)	6.85 ± 0.02	1.13 ± 0.04	0.69 ± 0.04	0.72 ± 0.04
	(JL98)	6.97 ± 0.04	0.80 ± 0.08	0.65 ± 0.07	0.69 ± 0.04
	(TR98)	–	1.17 ± 0.05	0.68 ± 0.03	–
1996 TQ ₆₆	(This work)	7.17 ± 0.06	1.22 ± 0.13	0.69 ± 0.10	0.75 ± 0.10
	(TR98)	–	1.16 ± 0.10	0.70 ± 0.07	–
1996 TS ₆₆	(This work)	5.86 ± 0.03	1.10 ± 0.06	0.69 ± 0.05	0.62 ± 0.06
	(JL98)	6.11 ± 0.08	0.93 ± 0.09	0.43 ± 0.12	0.67 ± 0.12
1997 CQ ₂₉	(This work)	6.60 ± 0.07	0.99 ± 0.13	0.64 ± 0.11	0.57 ± 0.13
	(B00)	6.70 ± 0.05	0.99 ± 0.12	0.68 ± 0.06	0.62 ± 0.09
1997 CS ₂₉	(This work)	5.11 ± 0.03	1.16 ± 0.05	0.61 ± 0.05	0.66 ± 0.05
	(TR98)	–	1.08 ± 0.07	0.61 ± 0.04	–
	(B00)	4.88 ± 0.02	1.05 ± 0.06	0.66 ± 0.02	0.53 ± 0.04
1997 CU ₂₉	(This work)	6.22 ± 0.07	1.12 ± 0.14	0.59 ± 0.11	0.58 ± 0.13
	(B00)	6.16 ± 0.03	1.32 ± 0.12	0.61 ± 0.04	0.74 ± 0.06
1997 QH ₄	(This work)	6.88 ± 0.09	1.05 ± 0.18	0.65 ± 0.15	0.64 ± 0.16
	(TR00)	6.88 ± 0.06	1.01 ± 0.07	0.67 ± 0.05	–
2000 EB ₁₇₃	(This work)	4.61 ± 0.02	0.93 ± 0.04	0.65 ± 0.03	0.59 ± 0.03
	(F01)	4.72 ± 0.06	0.99 ± 0.14	0.60 ± 0.10	0.38 ± 0.09

Note. — References are as follows: B00 = Barucci *et al.* (2000); DMG97 = Davies, McBride and Green (1997); F01 = Ferrin *et al.* (2001); LJ96 = Luu and Jewitt (1996); M99 = McBride *et al.* (1999); TR98 = Tegler and Romanishin (1998); TR00 = Tegler and Romanishin (2000)

Table 6. Results of Bin Test

Sample	n^a	C_{min}^b	C_{max}^c	$C \pm \sigma_C^d$	m^e	$P(n, m)^f$	S^g
TR98	13	0.73	1.45	1.11 ± 0.08	1	0.033	0.967
TR00	19	0.80	1.41	1.14 ± 0.04	8	0.133	0.867
TR98+TR00	32	0.73	1.45	1.13 ± 0.05	8	0.127	0.873
This Work	28	0.81	1.49	1.16 ± 0.04	10	0.150	0.850

^aNumber of data points in the sample

^bMinimum value of color index

^cMaximum value of color index

^dMean and standard deviation on the mean

^eNumber of objects in central bin

^fProbability that m objects would be found in the central color bin from a sample of n objects drawn from a uniform distribution, from Equation 7

^gStatistical significance $S = 1 - P(n, m)$. Note that $S = 0.997$ corresponds to 3σ confidence.

Table 7. Results of Dip Test

Sample	Color	n^a	Dip statistic	S^b
TR98	B-V	13	0.13736	0.983
TR98	V-R	16	0.13542	0.993
TR00	B-V	19	0.05263	0.040
TR00	V-R	21	0.09921	0.933
This Work	B-V	28	0.06766	0.584
This Work	V-R	28	0.05555	0.239
This Work	R-I	28	0.06790	0.597

^aNumber of data points

^bStatistical significance $S = 0.9970$ corresponds to the nominal 3σ criterion for a statistically significant bimodality

Table 8. Results of Interval Distribution Test

Sample	Color	n^a	LI_o^b	$P(LI > LI_o)^c$
TR98	$B - V$	13	0.25	0.012
TR98	$V - R$	16	0.13	0.062
TR00	$B - V$	19	0.08	0.974
TR00	$V - R$	21	0.10	0.245
This Work	$B - V$	28	0.12	0.924
This Work	$V - R$	28	0.10	0.990
This Work	$R - I$	28	0.09	0.878

^aNumber of data points

^bLargest Interval in the sample

^cProbability that a Largest Interval greater than the one observed would be produced by chance from data selected at random from a uniform distribution. $P = 0.003$ corresponds to the nominal 3σ criterion for statistical significance.

Table 9. Observational Parameters of Spectra

UT Date	Instrument	Object	λ [μm]	Slit Width [arcsec]	$\lambda/\Delta\lambda$	Seeing [arcsec]	τ_{CSO}	Int ^a [sec]
KECK I								
1998-11-13	NIRC	1993 SC	HK	0.68	~ 100	0.6	0.06	6000
1998-11-13	NIRC	1996 TS ₆₆	JH	0.68	~ 100	0.6-0.7	0.22	3600
1998-11-13	NIRC	1996 TS ₆₆	HK	0.68	~ 100	0.6-0.7	0.22	3600
1999-04-3,4	NIRC	1999 DE ₉	JH	0.68	~ 100	0.6	0.10-0.04	3000
1999-04-3,4	NIRC	1999 DE ₉	HK	0.68	~ 100	0.6	0.10-0.04	6000
SUBARU								
2000-06-18	CISCO	2000 EB ₁₇₃	JH	1.0	~ 1000	0.4	0.07	1440
2000-06-18	CISCO	2000 EB ₁₇₃	HK	1.0	~ 1000	0.4	0.07	2880

^aAccumulated integration time

Table 10. Infrared Reflectivities

λ^a	1999 DE ₉	2000 EB ₁₇₃	1996 TL ₆₆	1996 TS ₆₆	1993 SC
1.1	0.820 ± 0.009	1.040 ± 0.007	1.216 ± 0.054	0.529 ± 0.066	–
1.2	0.902 ± 0.010	1.040 ± 0.008	1.149 ± 0.041	0.587 ± 0.033	–
1.3	0.963 ± 0.011	1.053 ± 0.009	1.176 ± 0.041	0.645 ± 0.058	–
1.4	0.958 ± 0.013	1.075 ± 0.015	1.230 ± 0.068	0.570 ± 0.074	–
1.5	1.004 ± 0.010	1.107 ± 0.013	1.149 ± 0.041	0.744 ± 0.033	0.835 ± 0.165
1.6	1.003 ± 0.007	1.036 ± 0.014	1.243 ± 0.027	0.636 ± 0.066	0.824 ± 0.154
1.7	1.053 ± 0.013	1.023 ± 0.015	1.108 ± 0.041	1.008 ± 0.058	1.319 ± 0.132
1.8	1.060 ± 0.012	0.988 ± 0.034	1.203 ± 0.054	0.587 ± 0.107	0.868 ± 0.308
1.9	1.000 ± 0.017	1.007 ± 0.028	1.068 ± 0.054	0.496 ± 0.107	1.011 ± 0.187
2.0	0.959 ± 0.013	0.932 ± 0.021	1.014 ± 0.041	0.694 ± 0.074	1.308 ± 0.165
2.1	1.005 ± 0.009	0.936 ± 0.015	1.027 ± 0.041	0.917 ± 0.058	0.923 ± 0.110
2.2	1.000 ± 0.016	1.000 ± 0.018	1.000 ± 0.027	1.000 ± 0.074	1.000 ± 0.121
2.3	0.967 ± 0.015	0.978 ± 0.026	1.000 ± 0.041	0.851 ± 0.116	1.011 ± 0.154
2.4	0.945 ± 0.017	1.122 ± 0.040	0.946 ± 0.068	0.810 ± 0.174	0.769 ± 0.297

^aCentral wavelength of the bin (μm).

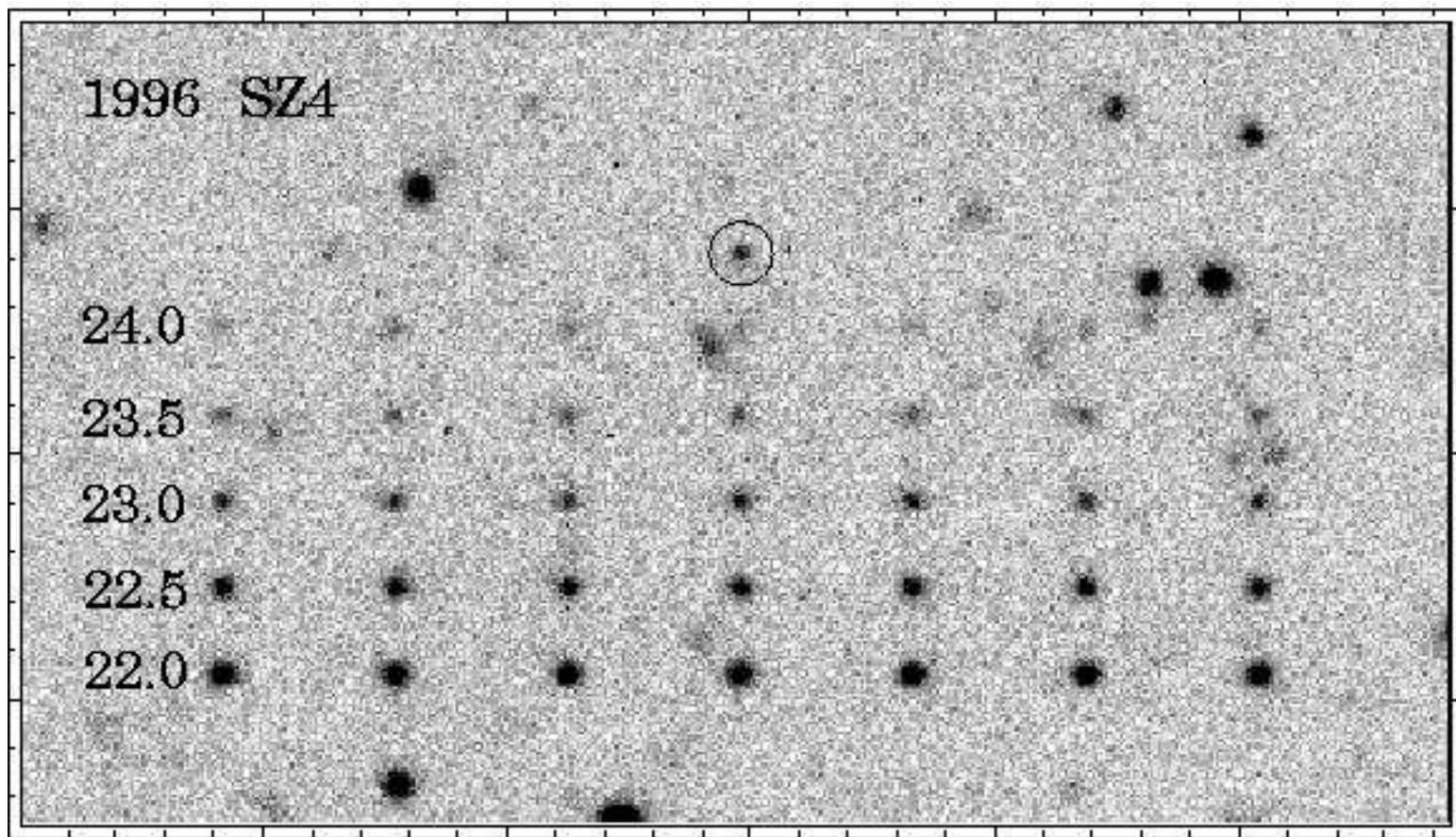


Figure 1

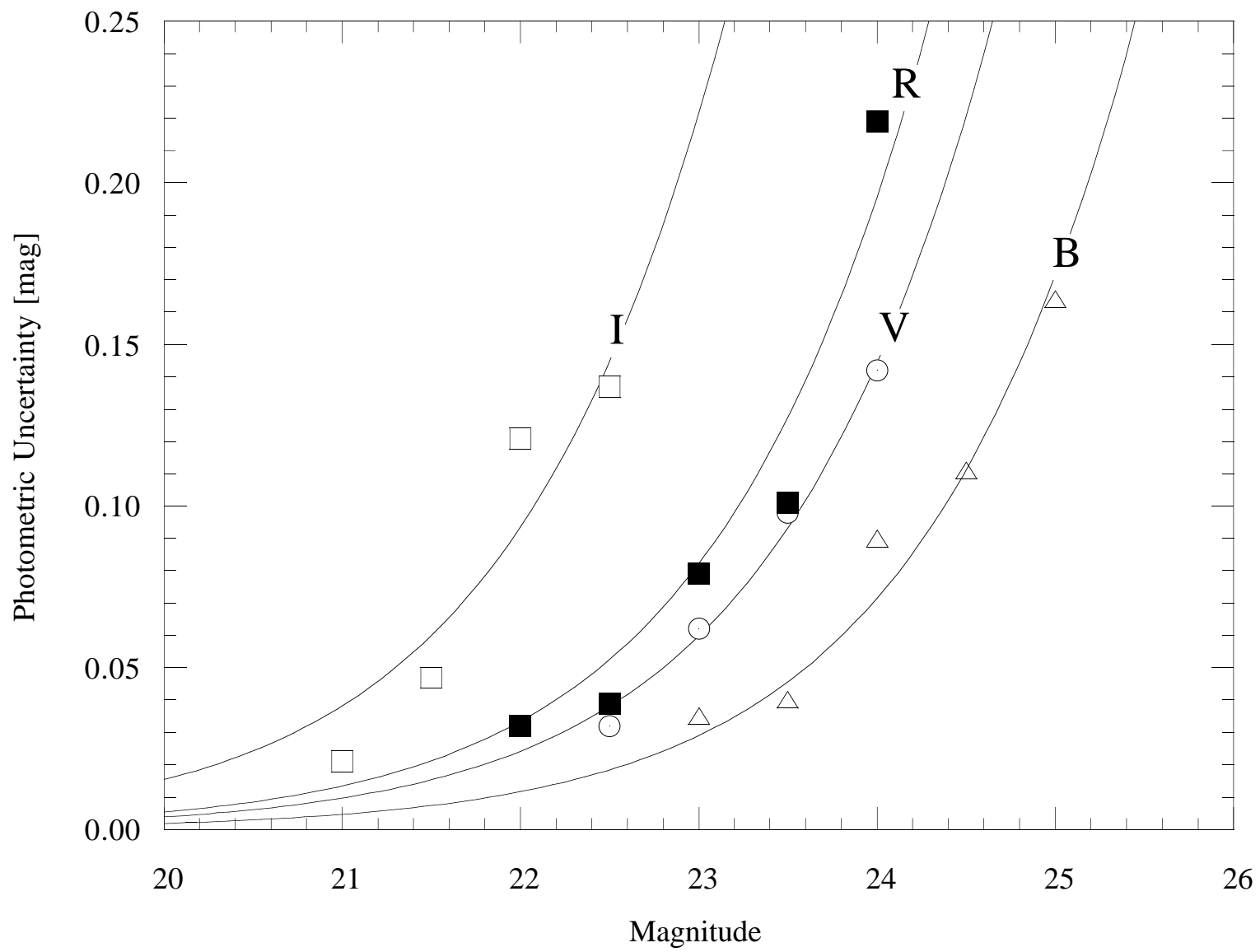


Figure 2

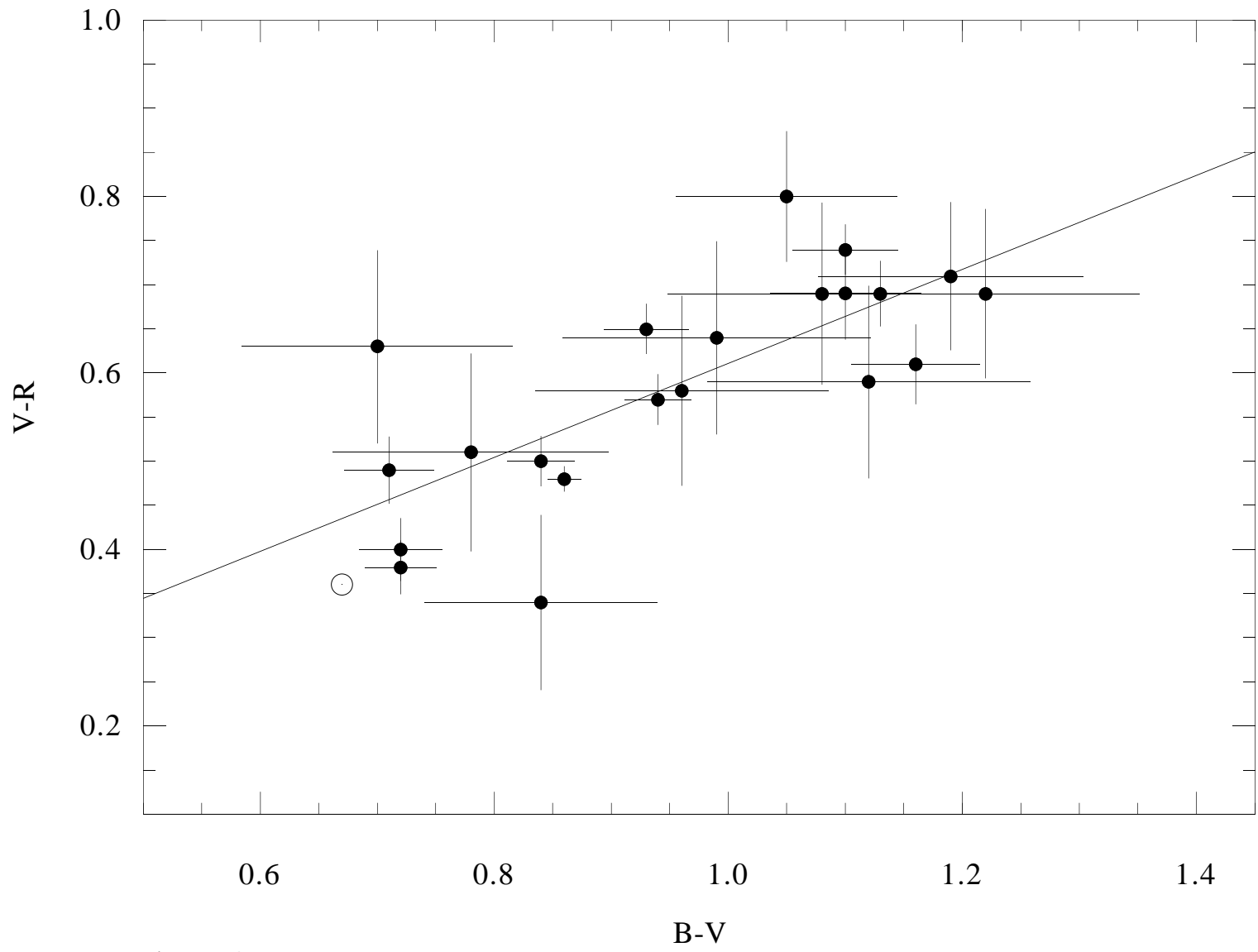


Figure 3

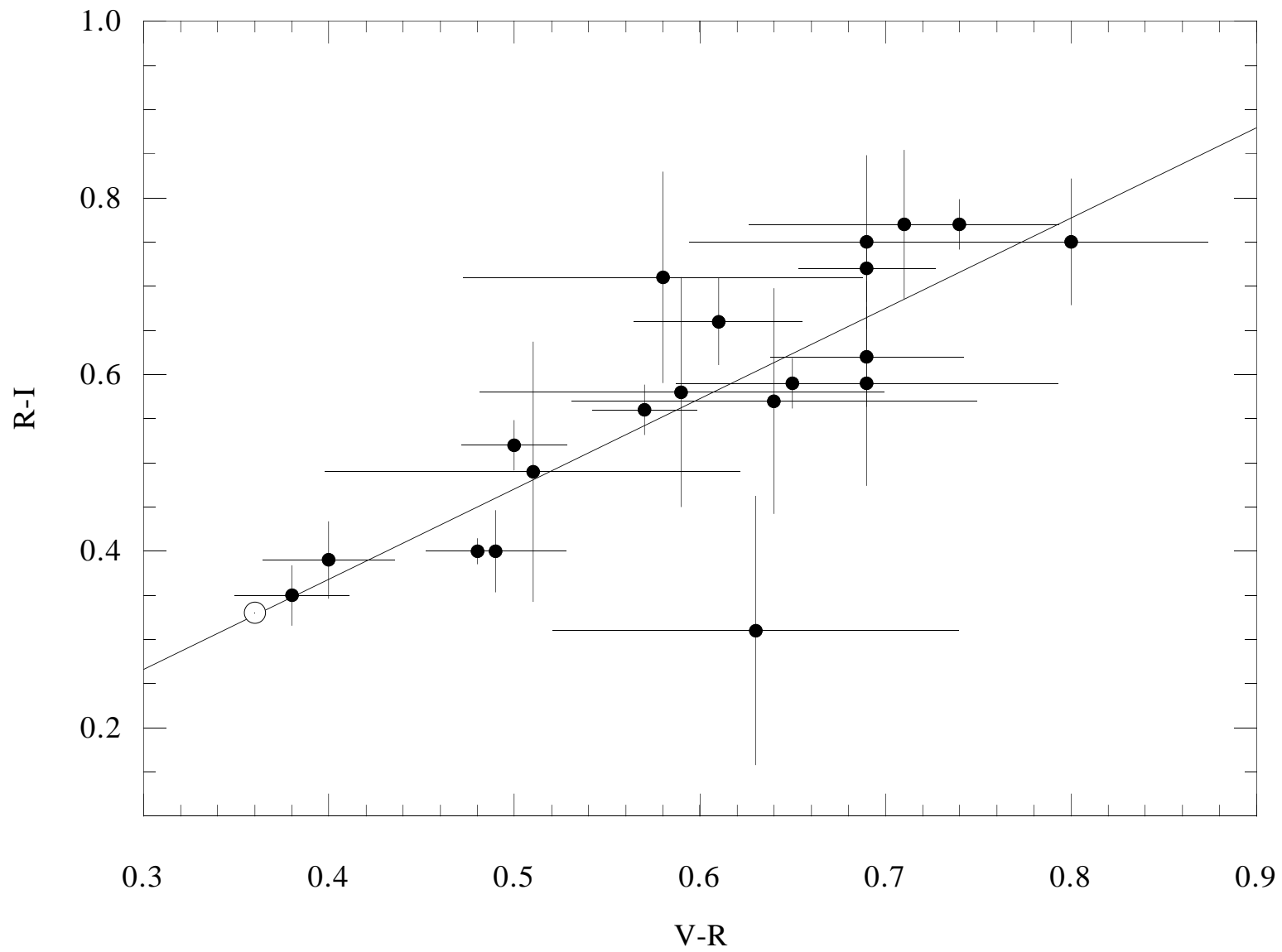


Figure 4

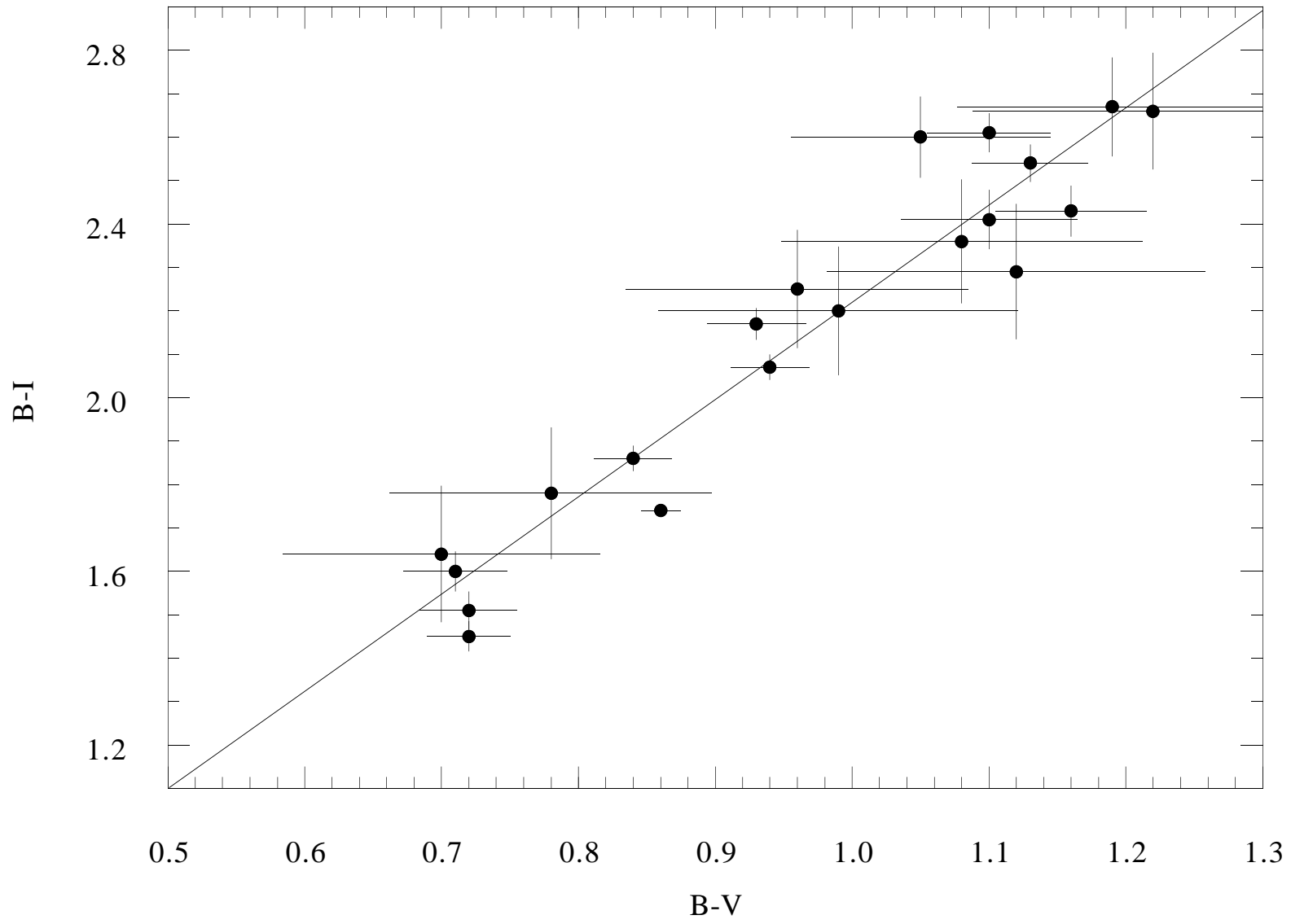


Figure 5

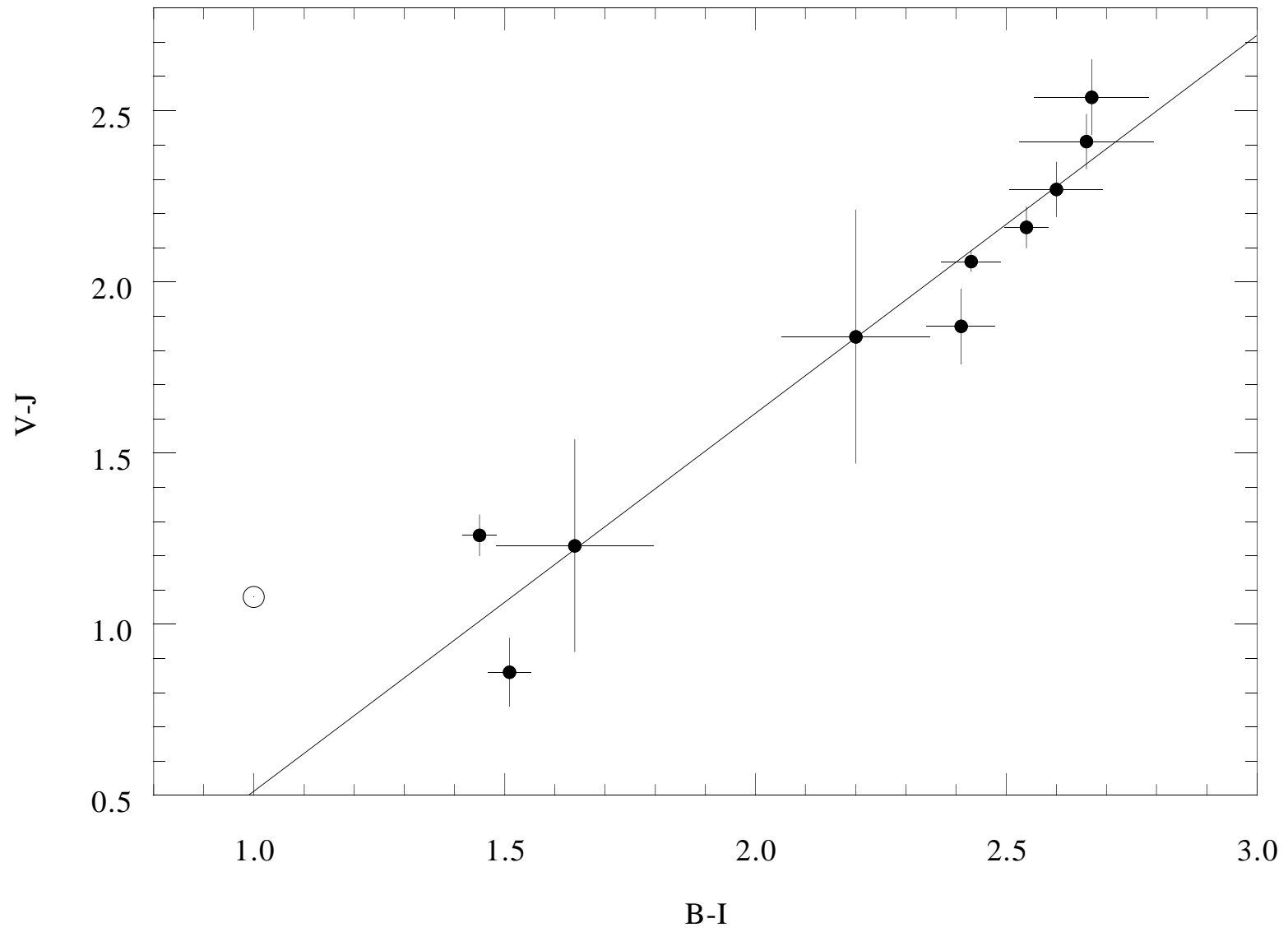


Figure 6

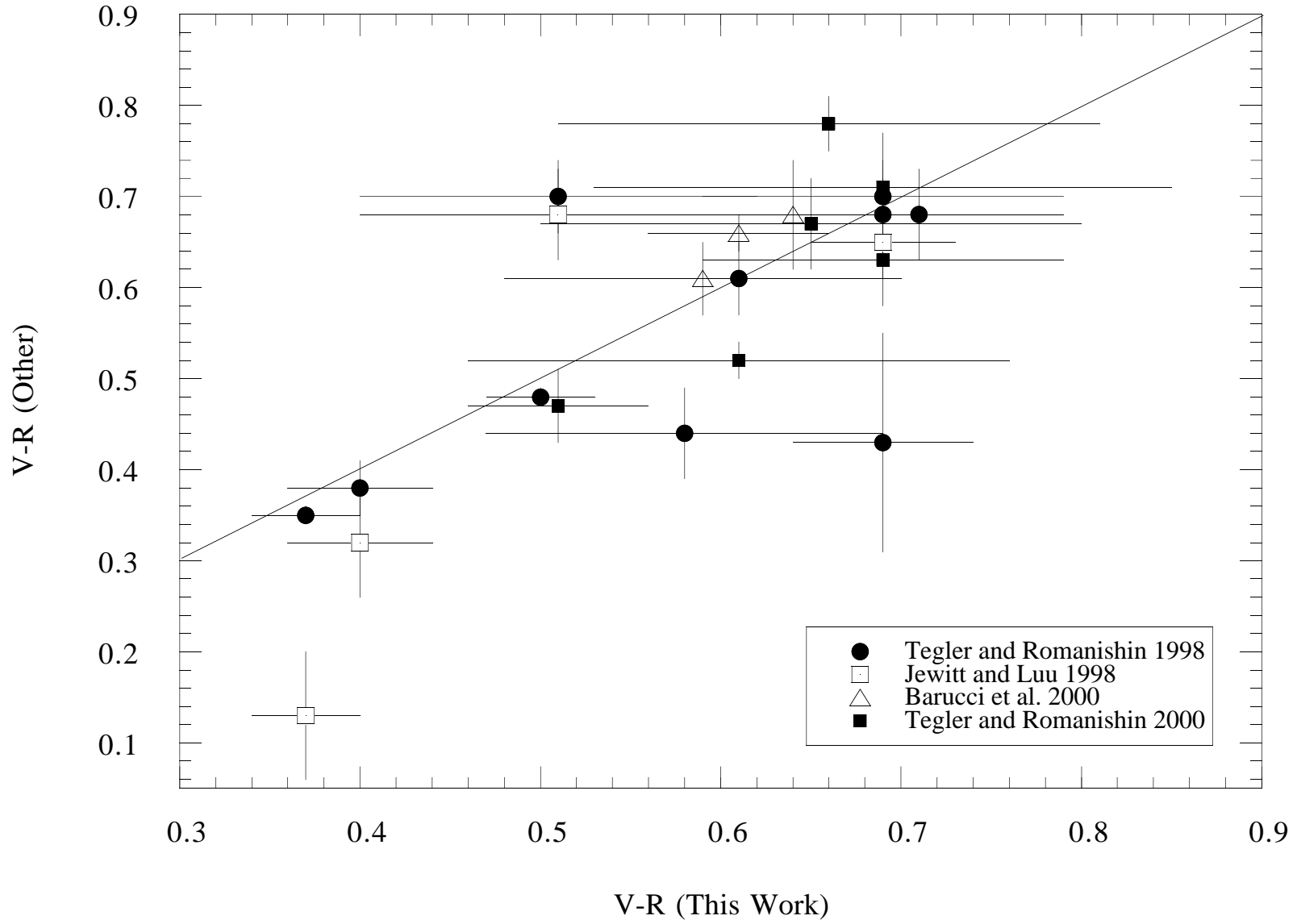


Figure 7

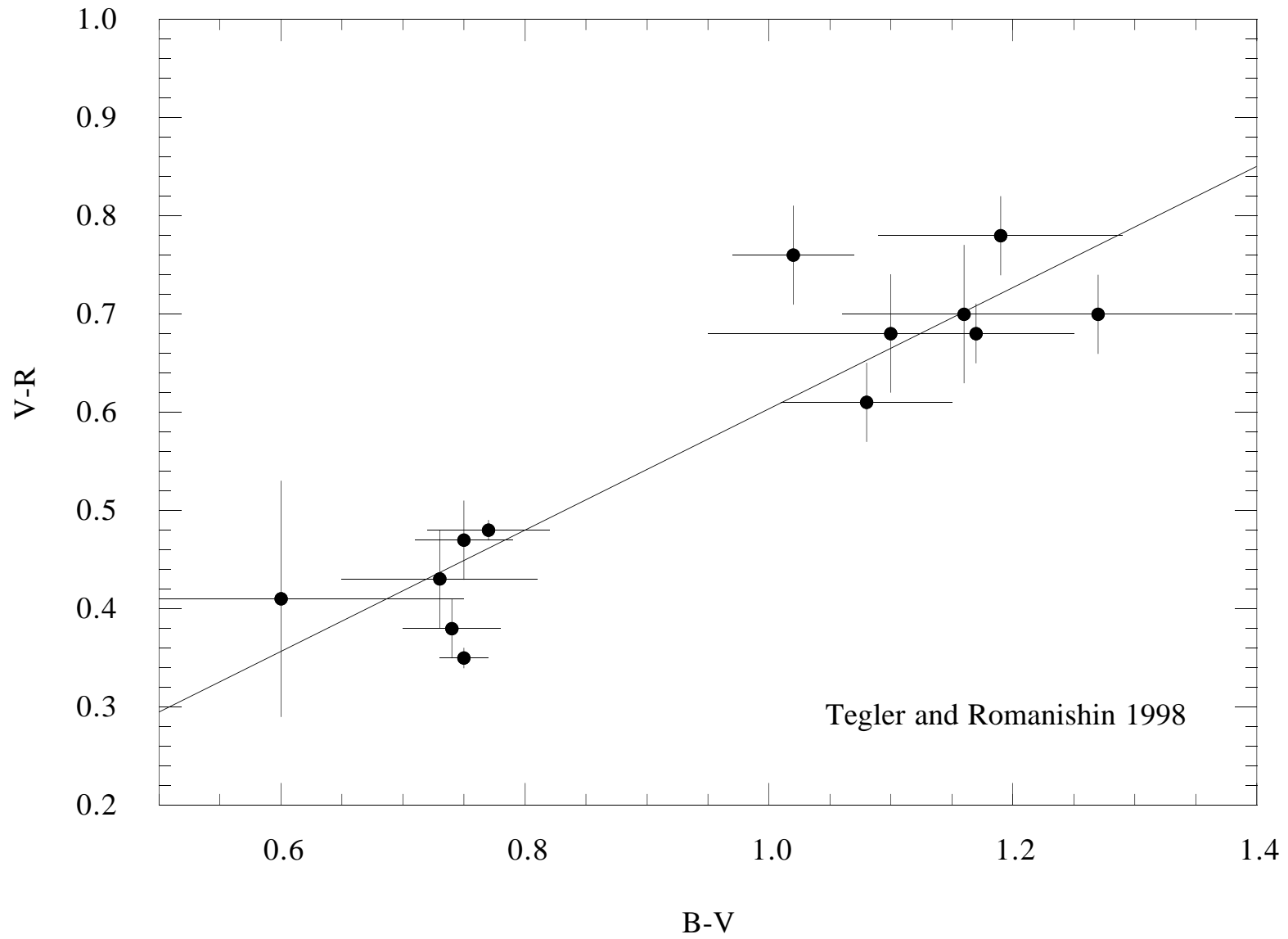


Figure 8

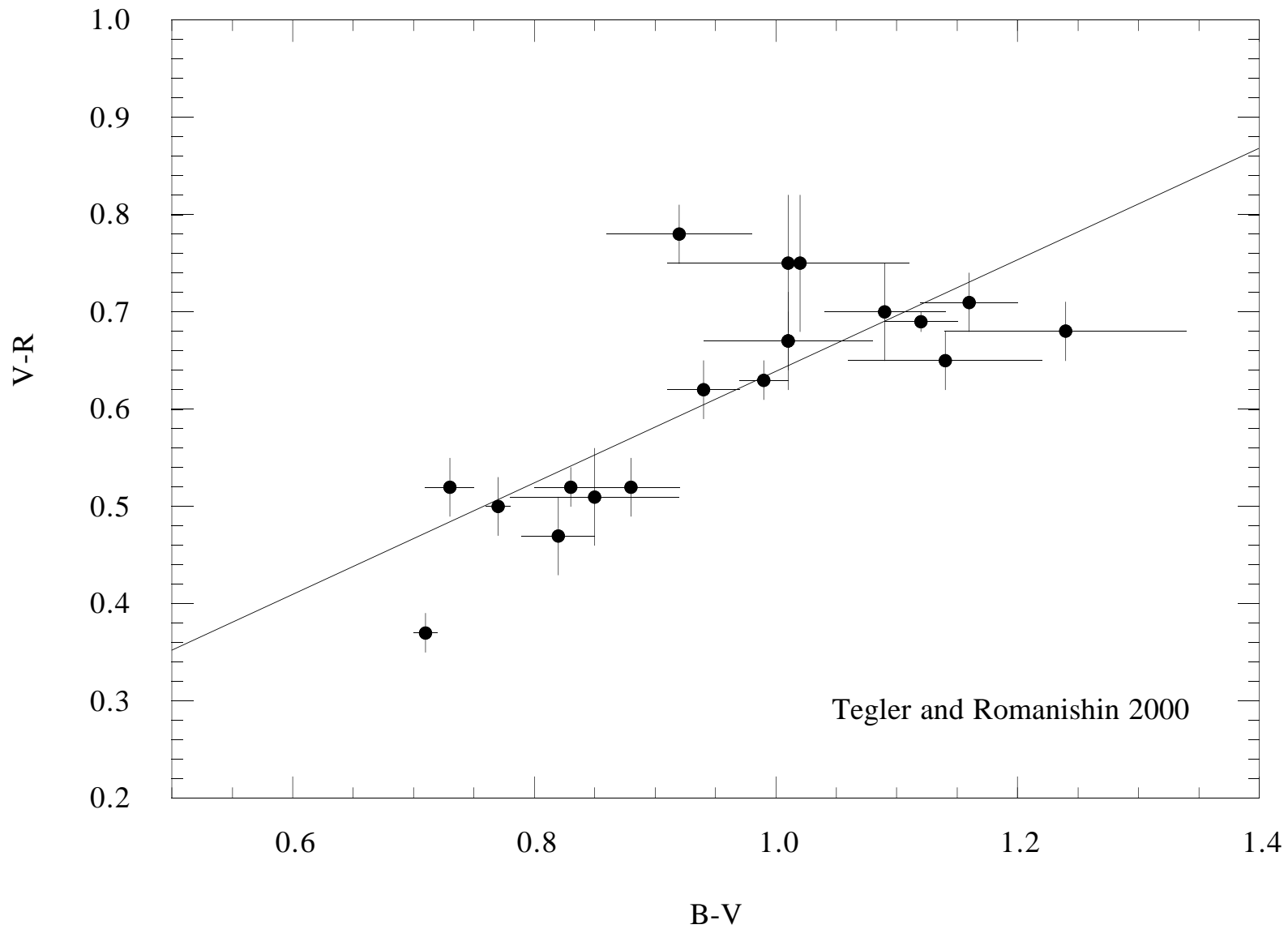


Figure 9

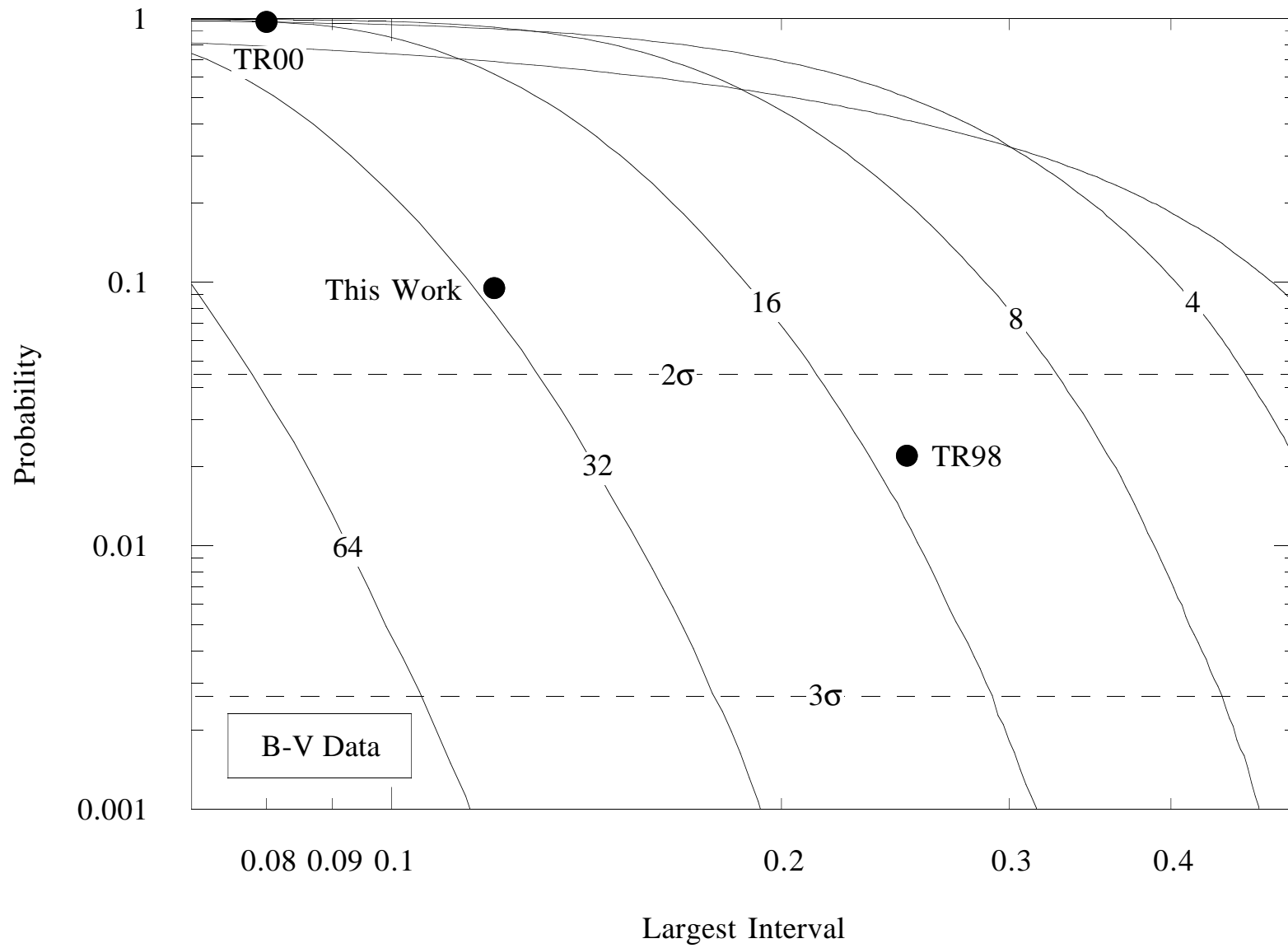


Figure 10

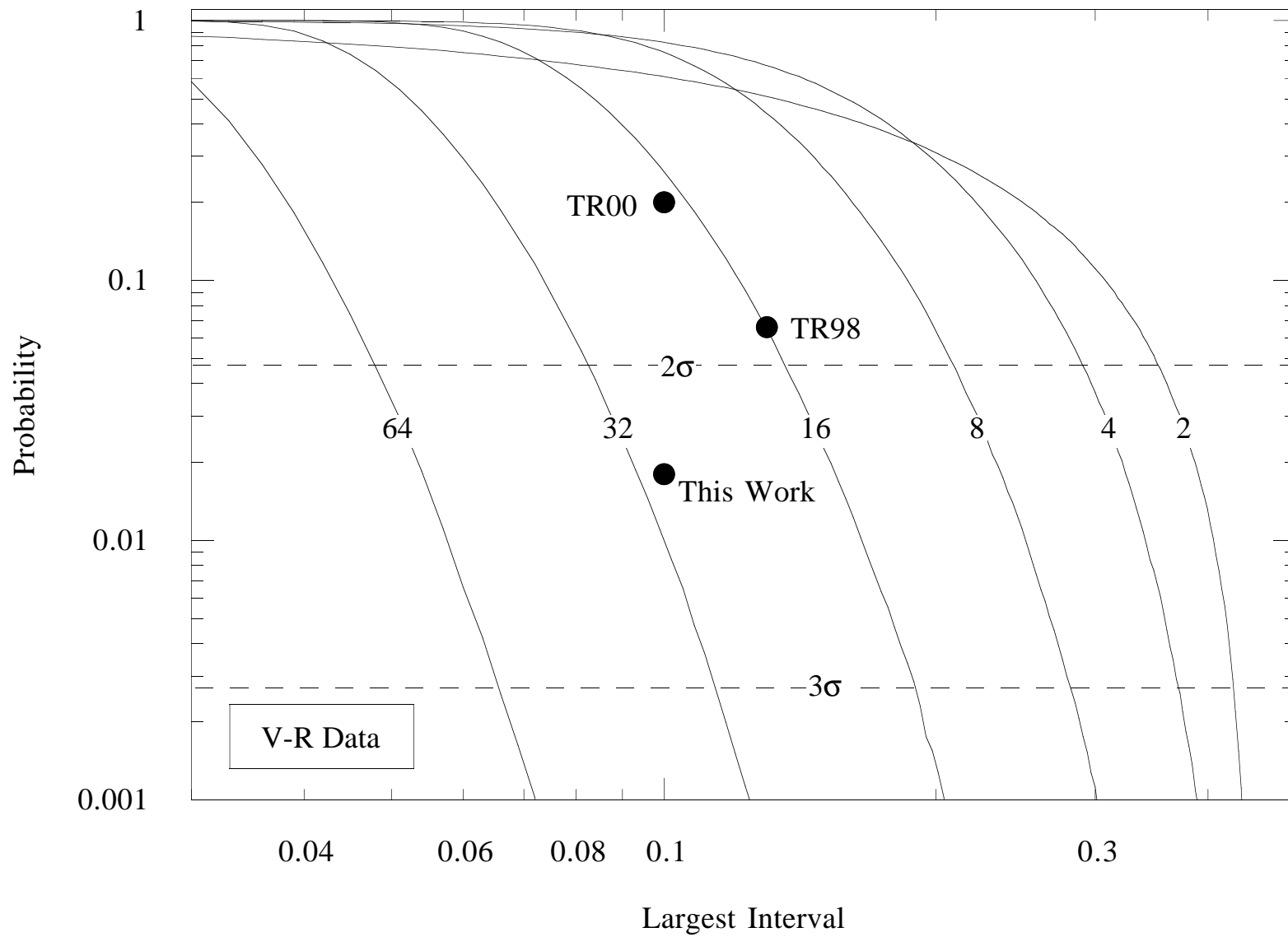


Figure 11

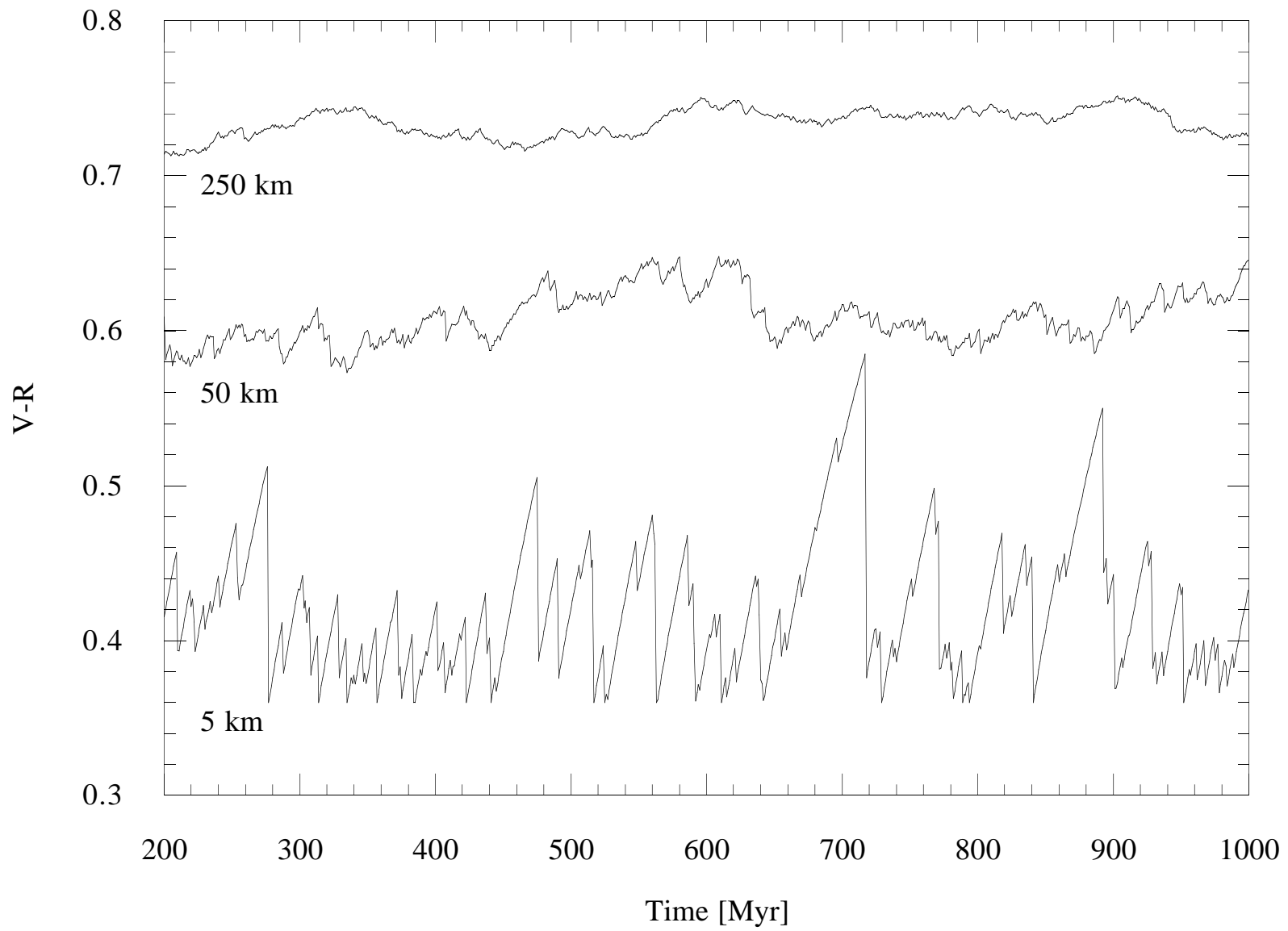


Figure 12

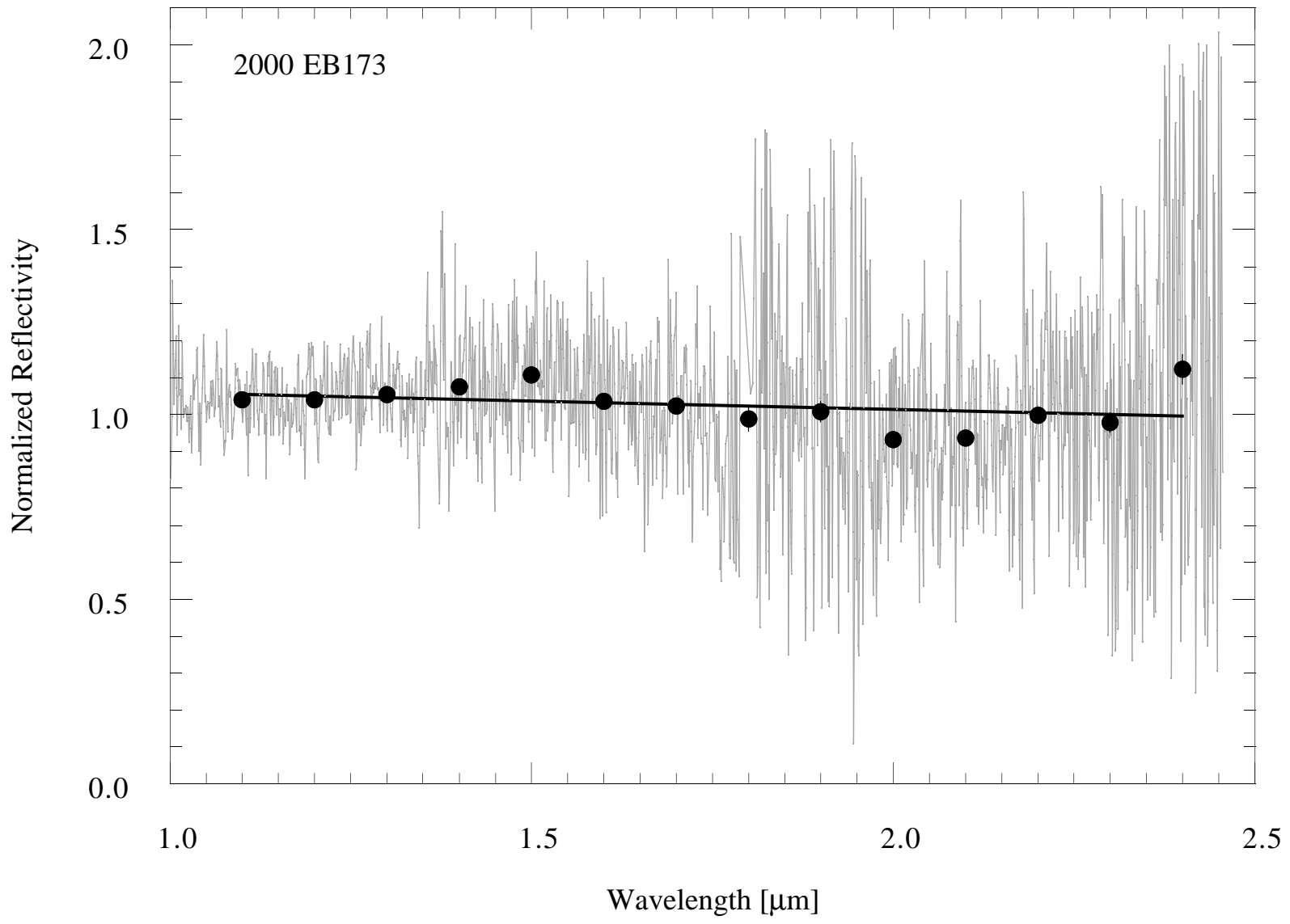


Figure 13

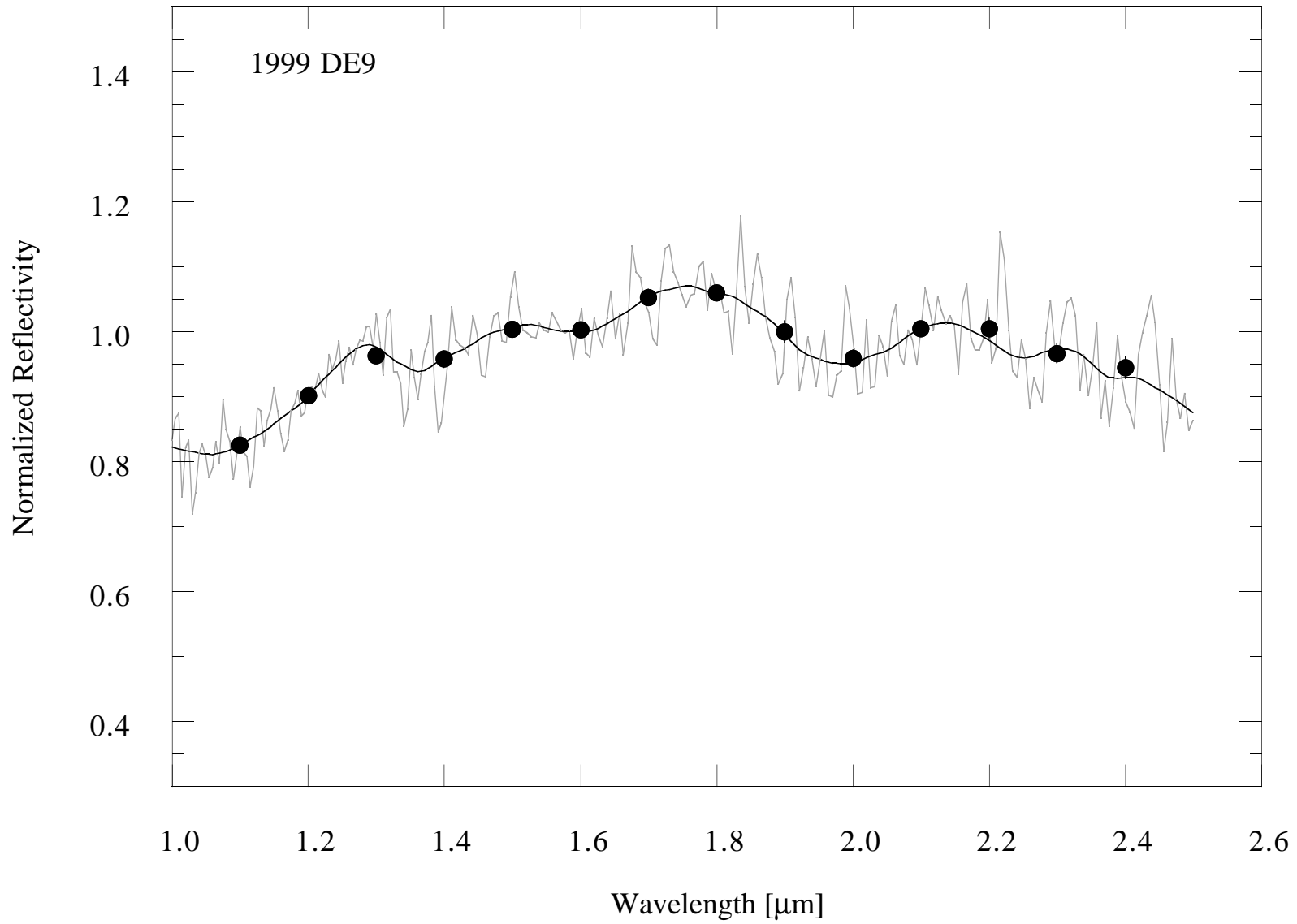


Figure 14

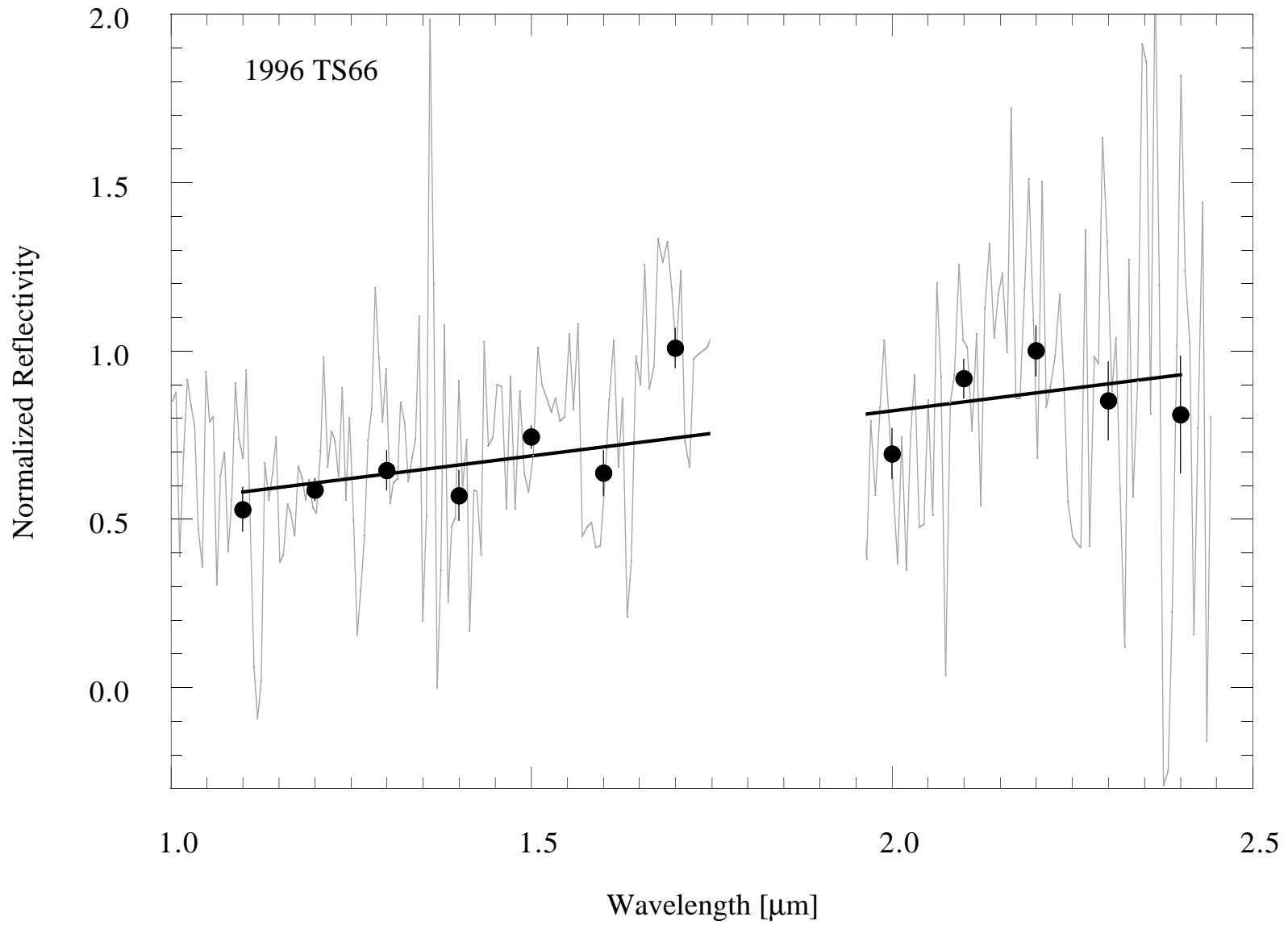


Figure 15

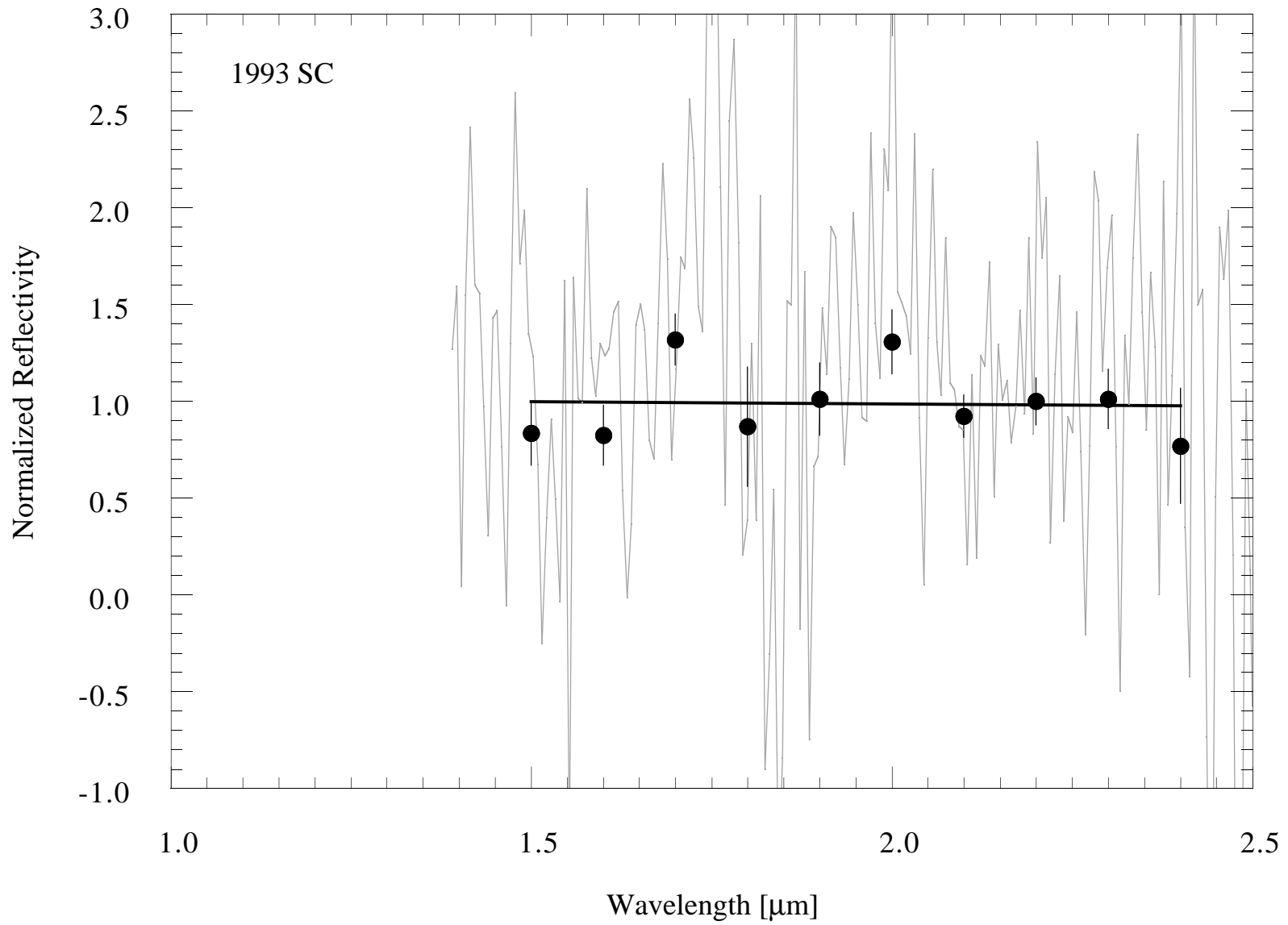


Figure 16

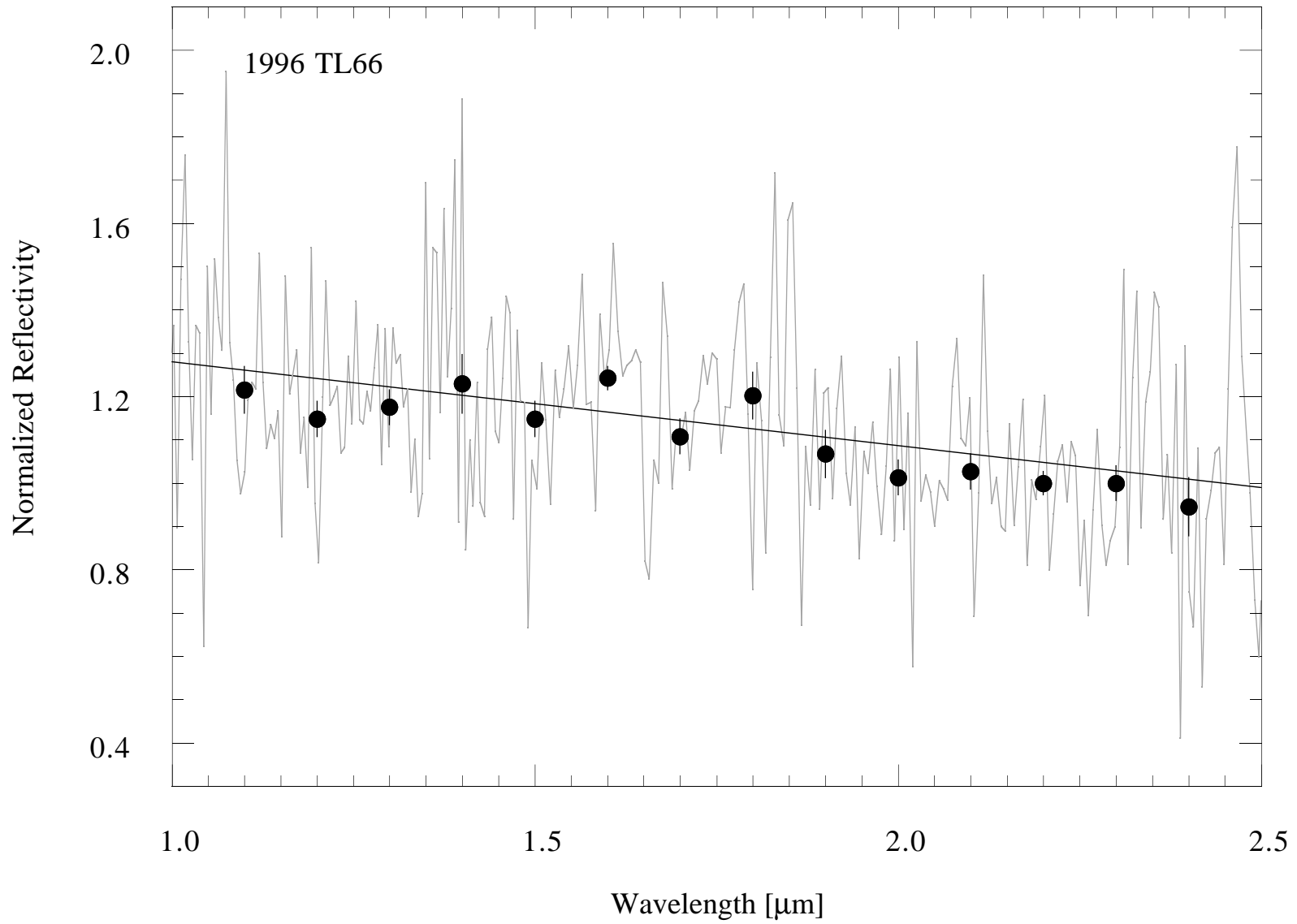


Figure 17

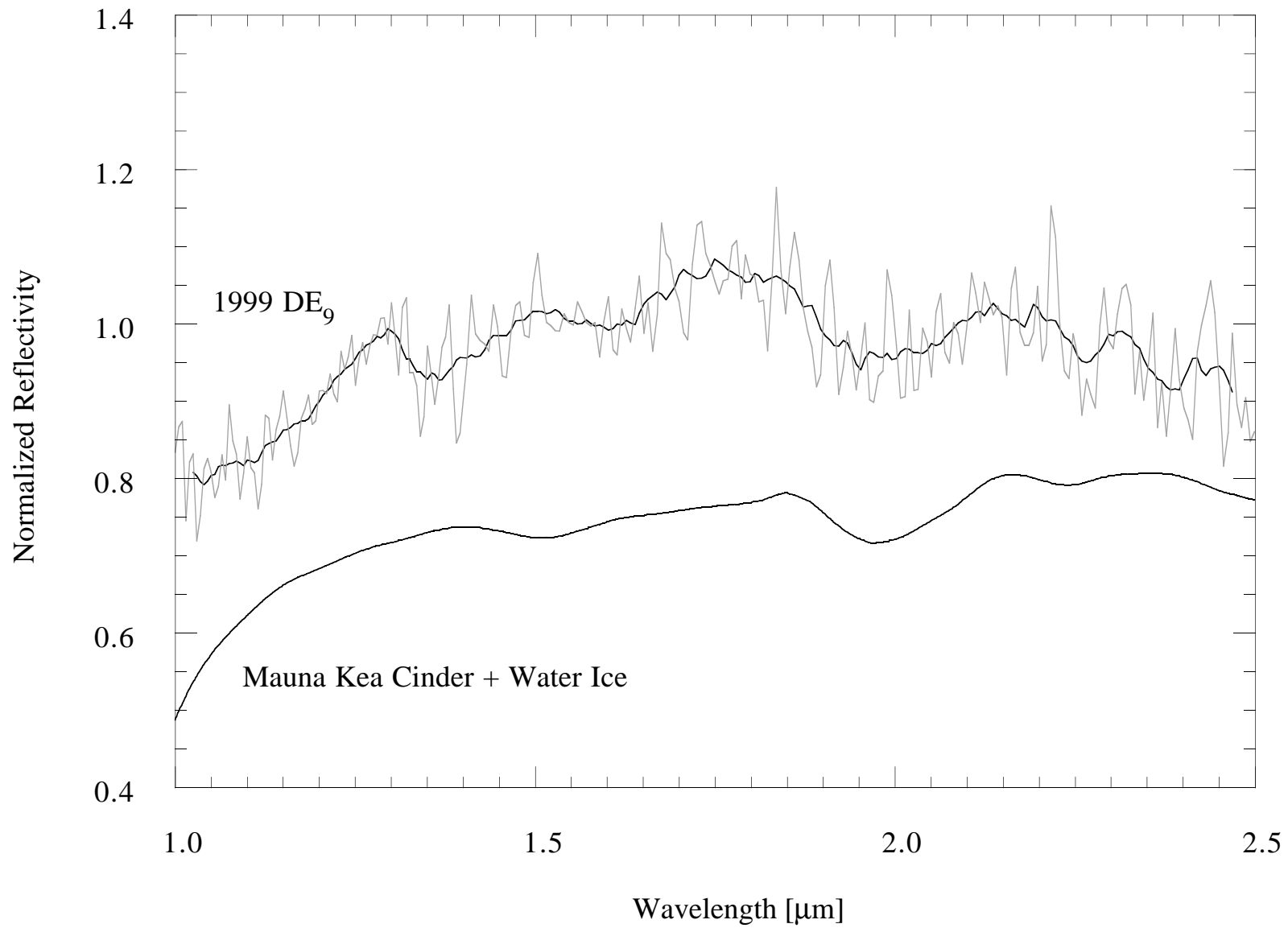


Figure 18

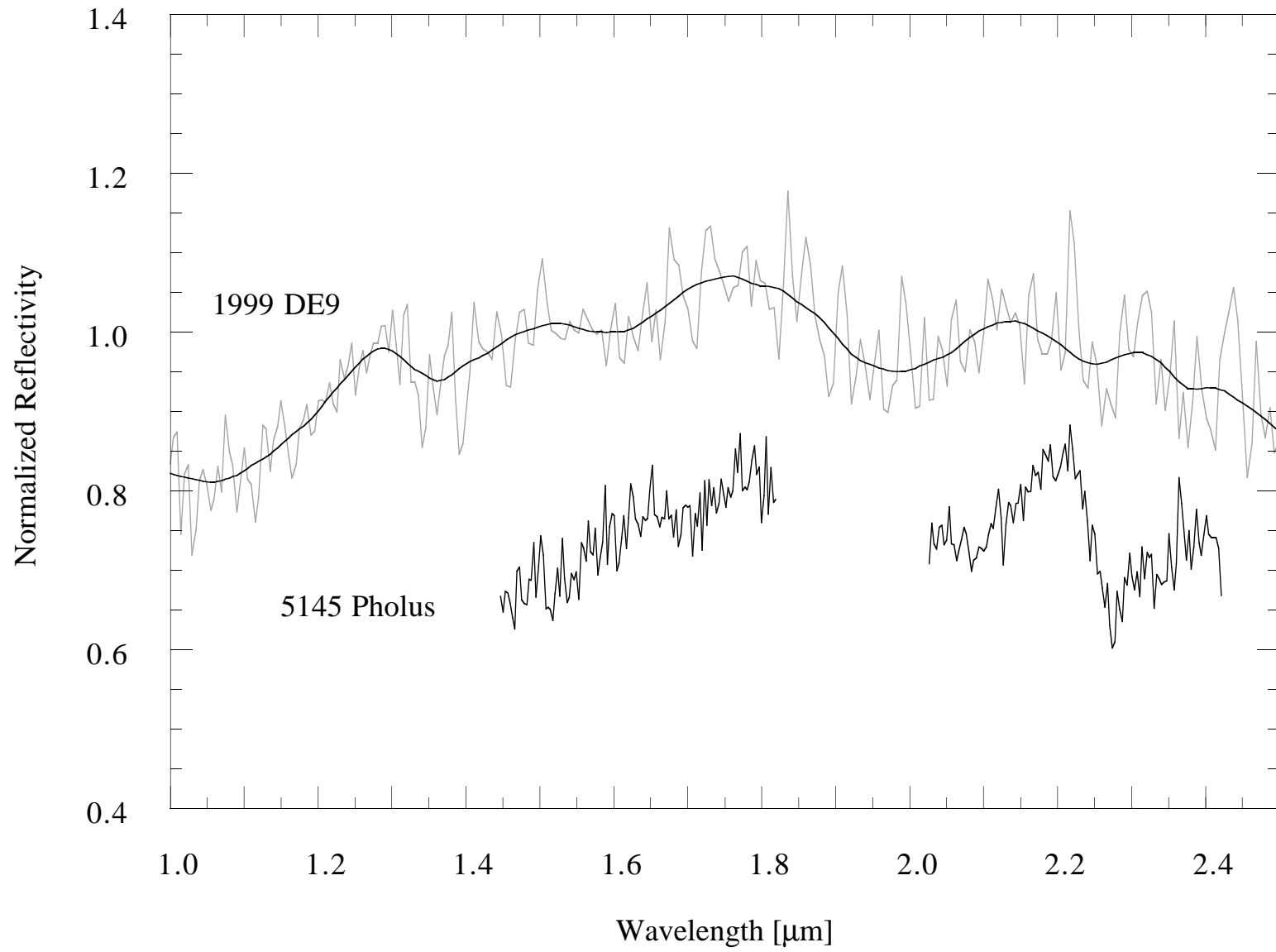


Figure 19